Catena 264 (2026) 109791

Contents lists available at ScienceDirect

Catena

journal homepage: www.elsevier.com/locate/catena

Topography and rainfall variability shaping dryland vegetation self-organisation: Insights from a numerical modelling study☆

Daniel Caviedes-Voullième [a,b,c,*], Yolanda Pueyo [d], Christoph Hinz [e]

[a] Simulation and Data Lab. Terrestrial Systems, Jülich Supercomputing Centre, Forschungszentrum Jülich, Jülich, Germany
[b] Institue of Bio- and Geosciences, Forschungszentrum Jülich, Jülich, Germany
[c] Chair of Environmental Fluid Dynamics and Modeling, Technical University of Dresden, Dresden, Germany
[d] Instituto Pirenáico de Ecología (CSIC), Zaragoza, Spain
[e] Chair of Hydrology - Brandenburg University of Technology, Cottbus, Germany

ARTICLE INFO

Keywords:
Banded vegetation
Hillslope shape
Vegetation self-organisation
Ecohydrology
Water-limited ecosystem

ABSTRACT

The coevolution of hydrological and vegetation dynamics in semi-arid regions often leads to vegetation self-organisation (VSO). While numerous hypotheses on the ecohydrological processes driving VSO have been explored through mathematical models, these have struggled to capture the multiscale complexity emerging from short-term surface runoff over heterogeneous topographies under variable rainfall. This limitation hinders understanding of how natural topography and rainfall variability shape long-term vegetation patterns.

Previous studies suggest that intra-storm water redistribution at the hillslope scale – controlled by topography and storm intensity – plays a key role in VSO. However, these factors have rarely been considered together due to methodological constraints in numerical solvers. We argue that accurately representing these processes is essential to investigate their interactions.

This study systematically examines the effects of hillslope topography and intra-annual rainfall distributions on vegetation band formation using a physically based model that couples the Zero-Inertia (Diffusive Wave) approximation of the shallow water equations with the HilleRisLambers–Rietkerk vegetation model. Idealised 30-year simulations were conducted at second-scale hydrodynamic resolution across different hillslope forms (plane, convex, concave), slopes, and rainfall regimes along a semi-arid gradient.

Results show that both topography and rainfall variability strongly influence band formation through their control on water redistribution and hydrological balance. Steeper slopes enhance runoff over infiltration, reducing water availability and altering band geometry and migration. Concave hillslopes exhibit distinct runoff convergence and redistribution patterns compared to plane or convex slopes. Rainfall intermittency interacts with topography to further affect pattern stability and morphology. While both drivers shape pattern characteristics differently, their joint effects mainly influence band migration without providing a strong stabilising mechanism.

These results demonstrate the feasibility of long-term, physically based ecohydrological simulations, paving the way for more comprehensive models including sediment transport and geomorphic feedbacks.

1. Introduction

1.1. Vegetation self-organisation

Vegetation self-organisation (VSO) into bands (also known as arcs or stripes) is a well-known phenomena in semi-arid hillslopes around the world (Deblauwe et al., 2008; Valentin et al., 1999). It has been documented extensively in Australia (Dunkerley, 1997), Somalia (Macfadyen, 1950), Sudan (Deblauwe et al., 2011), Niger (Valentin and d'Herbès, 1999), Spain (Bergkamp et al., 1999), Mexico (Montaña, 1992) and the USA (Pelletier et al., 2012; Penny et al., 2013). VSO and its interactions with soil and water have received wide attention both from field (e.g. Barbier et al., 2006; Bergkamp et al., 1999; Couteron et al., 2000; Dunkerley, 2002a; Gowda et al., 2018; Leprun, 1999; Puigdefábregas, 2005; Wu et al., 2000) and modelling studies (e.g. Baartman et al., 2018; Dunkerley, 1997; Esteban and Fairén, 2006; Foti and Ramírez, 2013; Klausmeier, 1999; Rietkerk et al., 2002; Saco

☆ This article is part of a Special issue entitled: 'landscape (co)evolution' published in Catena.

* Correspondence to: Wilhelm Johnen Strasse. 52425, Jülich, Germany.
E-mail address: d.caviedes.voullieme@fz-juelich.de (D. Caviedes-Voullième).

https://doi.org/10.1016/j.catena.2026.109791
Received 9 October 2025; Received in revised form 11 December 2025; Accepted 2 January 2026
Available online 17 January 2026

and Moreno de las Heras, 2013; Sherratt, 2016; Stewart et al., 2014; Thompson and Katul, 2009; Vega and Montaña, 2011; Yizhaq et al., 2005). VSO is a multiscale phenomenon arising from small scale interaction which result in large scale organisation. It is well accepted that bands form mainly due to scale-dependent feedbacks between water, soil and vegetation, interacting through water-redistribution mechanisms (Aguiar and Sala, 1999; McDonald et al., 2009; Sherratt, 2016) which operate at a variety of spatiotemporal scales. Additional factors (some of which depend strongly on hydrodynamics, e.g., nutrient transport, soil erosion, surface properties and processes) have been suggested to play a supporting role (Foti and Ramírez, 2013; Penny et al., 2013). A key insight from the body of research is the consensus that VSO can generate bands without underlying spatial heterogeneity (Rietkerk et al., 2002; Barbier et al., 2006; Pelletier et al., 2012; Zelnik et al., 2013). Notwithstanding, heterogeneity can trigger/inhibit similar mechanisms (Kästner et al., 2024, 2025; Köhnke and Malchow, 2017; McGrath et al., 2012; Sun et al., 2013).

1.2. Drivers and complexity

VSO is an emergent landscape-scale phenomenon arising from interactions at smaller spatiotemporal scales. Dominant among these are surface runoff dynamics – occurring over metres and minutes (Dunkerley, 2018c; Pappas et al., 2015) – which control local water redistribution and hydrological partitioning (Svoray et al., 2021). Vegetation establishment locally enhances infiltration, further modifying water flow. Combined with slower processes such as subsurface water movement and vegetation dynamics at kilometre and century scales (Eddy et al., 1999; Sherratt, 2015), this feedback drives the formation of banded vegetation patterns (Baartman et al., 2018; Gandhi et al., 2018; Paschalis et al., 2016; Saco et al., 2018).

Two dominant factors underpin the complexity of these hydrodynamics—and thus VSO: topography and rainfall. Topography is central to VSO's multiscale nature, linking sub-band processes to the landscape scale. Most studies focus on the influence of the average regional slope – defined over distances much greater than the interband width (Pelletier et al., 2012) – reporting correlations with band properties (Baartman et al., 2018; Deblauwe et al., 2008; Eddy et al., 1999; Gowda et al., 2018; Pelletier et al., 2012; Penny et al., 2013; Sherratt, 2015; Valentin et al., 1999). In contrast, fewer studies have examined how hillslope shapes or complex topographies influence patterns (Dunkerley and Brown, 1999; Gandhi et al., 2018; Pelletier et al., 2012; Penny et al., 2013), often due to data limitations or model simplifications.

Small-scale heterogeneities and local slopes shape runoff pathways (McGrath et al., 2012) and VSO itself (Dunkerley, 1997; Dunkerley and Brown, 1999; Eddy et al., 1999; Pelletier et al., 2012; Valentin and d'Herbès, 1999). Hillslope longitudinal shape affects band number and wavelength (Baartman et al., 2018; Foti and Ramírez, 2013), while cross-sectional topography (e.g., valleys and ridges) shapes band curvature and alters the rainfall range for pattern emergence (Gandhi et al., 2018), highlighting the relevance of topographic structure across multiple scales.

Rainfall is another key VSO driver (Deblauwe et al., 2008; Meron et al., 2004; Meron, 2018). Annual precipitation – a proxy for aridity – defines transitions between spotted, labyrinth, and gap patterns in flatlands (Meron, 2016). On hillslopes, it determines a critical slope threshold above which bands form, and below which spotted patterns dominate (Deblauwe et al., 2011; Ursino, 2005; Valentin et al., 1999).

The relationship between rainfall and banding is well-documented (e.g. Couteron, 2002; Deblauwe et al., 2011; Gowda et al., 2018; Lefever and Lejeune, 1997; Lejeune et al., 2004; Sherratt, 2013, 2015; Siteur et al., 2014b). Temporal variability also shapes VSO (Guttal and Jayaprakash, 2007; Kletter et al., 2009; Ursino and Contarini, 2006), especially in drier systems (Djebou et al., 2015). Rainfall in drylands is highly seasonal and variable (McDonald et al., 2009; Trichon et al., 2018), and intra-storm dynamics drive runon–runoff interactions (Dunkerley, 2018a; Galle et al., 1999; Penny et al., 2013; Puigdefábregas, 2005), infiltration (Thompson et al., 2011), soil moisture patterns (Paschalis et al., 2016; Siteur et al., 2014a), and vegetation responses (Fernández, 2007). Inter-event variability, such as ephemeral ponding or excitation by frequent small or rare large events, also influences pattern formation (Dunkerley, 2018a; Eddy et al., 1999; Pelletier et al., 2012). Generally, intense and infrequent storms promote greater runoff connectivity and total runoff, modulated by infiltration heterogeneity (Moreno de las Heras et al., 2020), with these effects being scale-dependent in drylands (Mounirou et al., 2021). Rainfall variability (through water availability), affects long-term VSO dynamics (Caviedes-Voullième and Hinz, 2020; Trichon et al., 2018), resilience (Cueto-Felgueroso et al., 2015), resource connectivity (Stewart et al., 2014), intra-seasonal ecosystem responses (Schwinning et al., 2004), and species composition (Bates et al., 2006). Yet, many ecological responses to rainfall variability and the system's memory remain poorly understood (Ogle et al., 2015). Climate change may further amplify this variability in drylands (Grünzweig et al., 2022), potentially extending dryland-like dynamics to other regions (Groner et al., 2023).

1.3. Modelling approaches

Lean and rather idealised models have dominated the VSO literature (e.g. Borgogno et al., 2009; Klausmeier, 1999; Meron, 2018; Rietkerk et al., 2002; Zelnik et al., 2013) where processes are simplified to a bare minimum and the complexity of topography and rainfall is skimmed into extremely simple proxies, such as periodic slopes and constant rainfall respectively. This approach has been fruitful and insightful. Most of these models are not process-oriented (Dunkerley, 2018c), their variety (Borgogno et al., 2009) implies they cannot be all fully correct or complete (Dunkerley, 2018a), and translating them into meaningful interpretations of the processes and indicators remains a challenge (Borgogno et al., 2009; Caylor et al., 2009; Dunkerley, 2018a; Kéfi and Couteron, 2018; Paschalis et al., 2016; Stewart et al., 2014).

Arguably, to properly simulate the macroscale emergent VSO for the right microscale reasons (Bokulich, 2014), *multiscale* process-based models (PBM) are warranted (Crompton and Thompson, 2021; Fatichi et al., 2016). PBMs should include a full representation of surface and subsurface hydrodynamics – at the effective scales in which they occur (Caviedes-Voullième et al., 2021) –, together with a mechanistic representation of vegetation physiological processes including uptake, growth, mortality, and reproduction, and consequently better-defined parametrisations which lump and mask fewer processes (Penny et al., 2013; Ursino, 2005).

In the pursuit of a PBM framework for VSO, simple models have been augmented to better account for a breadth of processes, including energy feedbacks (Foti and Ramírez, 2013), physiology and water stress dynamics (Dunkerley, 2018a; Paschalis et al., 2016; Trichon et al., 2018; Ursino, 2007), biomass propagation (Eigentler and Sherratt, 2018; Pueyo et al., 2008; Saco et al., 2007; Thompson and Katul, 2009; Thompson et al., 2014) and land surface co-evolution (Saco et al., 2007; Saco and Moreno de las Heras, 2013). Paschalis et al. (2016) proposed an ambitious and perhaps the most complete mechanistic model in hydrological and physiological terms, although renouncing spatial vegetation reproductive dynamics and VSO. This comprehensive approach comes with high computational cost (Le and Kumar, 2017), and a bulky parametrisation. Similarly, physically-based hydrodynamics involving Richards and shallow water equations have been invoked (Crompton et al., 2019; Crompton and Thompson, 2021), to study hillslope responses, flow paths and connectivity in patterned vegetation Crompton et al. (2023). Crompton and Thompson (2021) used an emulator trained with such PBM to predict vegetation dynamics.

On top of these arguments, a significant part of the validation of the idealised VSO models has been based on qualitative pattern matching (Dunkerley, 2018a; Mander et al., 2017; Stewart et al.,

2014). Quantitative validation (DeAngelis, 2012) against site-specific pattern metrics is evermore necessary (Dunkerley, 2018a; Gowda et al., 2018). In order to address this challenge, the sources of complexity – i.e., topography, rainfall variability, among others – must be acknowledged (Bastiaansen et al., 2018; Dunkerley, 2018a; Gandhi et al., 2018; Stewart et al., 2014) in the models, thus making PBMs essential.

1.4. Surface flow in VSO models

Surface runoff dynamics have most often been represented with very simplified formulations in VSO models, most of which cannot account for hydrodynamics arising from complex topographies and variable rainfall. The base approach consists of linear diffusion or linear advection formulations (e.g. HilleRisLambers et al., 2001; Foti and Ramírez, 2013; Klausmeier, 1999; Rietkerk et al., 2002; Gilad et al., 2007; Thiery et al., 1995). These result in simple computational implementations and almost no numerical issues. The linear formulation allows to prescribe a stable, constant, and large (several minutes) time step size dominated by the rate of diffusion/advection for water and resolution, thus keeping computational effort low (i.e., runtimes of tens of minutes on a laptop). However, they completely neglect the non-linear nature of free-surface flows, cannot represent realistic topographies, are limited to homogeneous linear slopes, and the physical meaning of the diffusion/advection coefficients are – at best – unclear.

Kinematic wave (KW) approximations of the shallow water equations (SWE) together with steepest-descent flow paths have also been used (Baartman et al., 2018; Paschalis et al., 2016; Saco et al., 2007; Saco and Moreno de las Heras, 2013). KW neglects acceleration and pressure gradients, allowing only for gravity and friction to govern the flow. This somewhat more physical approach still disregards relevant small scale dynamics of surface flow and forgoes the possibility of solving transitions of hillslopes into flatlands – where the KW model degenerates –, an issue of potential importance, for example, in the degraded Sahel bands where runoff is transferred from hillslopes to flatlands (Trichon et al., 2018). Furthermore, KW may be inaccurate in representing dynamic flow paths (Baartman et al., 2018; McGrath et al., 2012; Saco and Moreno de las Heras, 2013) and the coarse (daily) time-step that is often associated with it cannot represent the intra-event runoff dynamics. Gilad et al. (2007) proposed a linearised diffusive wave approximation to the SWE with a linear friction term which does not suffer from the flatland limitation as the KW, but still fails to capture non-linearities of surface flows. Full SWE solvers have also been invoked, but with fixed, static vegetation (Pelletier et al., 2012; Crompton et al., 2019). SWE solvers have a much higher computational cost, for which machine-learning emulators have also been proposed (Crompton and Thompson, 2021; Crompton et al., 2023).

The linear models, with linear slopes have also imposed periodic boundary conditions at the upslope and downslope ends (Gilad et al., 2007; Klausmeier, 1999; Dagbovie and Sherratt, 2014; Esteban and Fairén, 2006; Pelletier et al., 2012; Sherratt, 2013, 2015, 2016; Stewart et al., 2014; Thiery et al., 1995; Ursino and Contarini, 2006; Ursino, 2007). In clear contrast, natural hillslopes have a clear hilltop (a water-divide) and a hillfoot, which is potentially a runoff outlet, as evidently observed in the fields and experiments (e.g., Moreno de las Heras et al., 2020; Svoray et al., 2021). Periodic boundaries – which disregard a net runoff loss (Siteur et al., 2014a) – have been shown to introduce artefacts, by comparing with non-periodic domains (Baartman et al., 2018; McGrath et al., 2012; Foti and Ramírez, 2013; Penny et al., 2013; Saco et al., 2007; Saco and Moreno de las Heras, 2013).

1.5. Research questions

This paper addressed the research gap that the two main drivers of hydrodynamic complexity (topography and rainfall variability) have not been studied together. We hypothesise that these drivers interact in various ways through the hydrodynamic response, in turn affecting the features and evolution of banded systems. We also hypothesise that different features of the banded system (e.g., wavelength, bandwidth, etc.) respond differently to the different combinations of drivers. We test our hypotheses by studying rainfall intermittency together with different hillslope profiles and different regional slopes on the ecohydrological response of banded vegetation, to assess the role that realistic hillslope shapes have on the response of system, in contrast to the simplified linear systems often represented. This study constitutes the first systematic analysis of the response of VSO to different non-linear hillslope profiles in combination with rainfall variability.

To represent the hydrodynamics in the VSO context, we propose an intermediate complexity PBM based on a multiscale physically-based surface flow model. We rely on the Zero-Inertia (ZI) approximation for surface flows. ZI allows to solve surface flow at small spatiotemporal scales (m^2 and seconds), while running simulations that are large and long enough (hectares, decades) to observe the emergent, larger-scale, VSO. We argue that ZI is a reasonable compromise between the commonly used very simple approaches for surface flow in VSO models, and the full physics of the SWE, but one which allows to explicitly account for topography, friction and pressure gradients. It also handles wetting and drying fronts, thus fully encompassing hydrodynamics in response to topography and rainfall variability. In this sense, we increase the *depth* of the representation of hydrodynamics, but choose not to increase the *breadth* in terms of further physiological and ecological processes, avoiding a large increase in complexity, while better representing key processes, arguably increasing accuracy and decreasing parametrisation uncertainty.

The combination of a process-based surface flow model with the Rietkerk model allows to substantially relax simplifying assumptions on hydrodynamics, and thus enables to simulate VSO over non-linear topographies with non-periodic boundaries (i.e., allowing for a runoff loss) with intermittent rainfall (which also allows for drying surfaces), at the appropriate spatiotemporal scales, is a strong methodological novelty of this work. In our approach we increase complexity only in surface hydrodynamics to pinpoint the effect that this has in the overall VSO model, although we acknowledge this may generate a mismatch in complexity. We argue that increasing complexity *one thing at a time* facilitates attribution of certain behaviours to driving processes and/or artefacts in their representation.

2. Mathematical and numerical model

The model is based on two hydraulic submodels (surface and subsurface flow) and a biomass evolution submodel. Biomass evolution is described by the diffusion-reaction PDE proposed by HilleRisLambers et al. (2001) and Rietkerk et al. (2002)

$$\frac{\partial b(\mathbf{x},t)}{\partial t} = \mathcal{G}(b,W) - \mathcal{F}(b) + \mathcal{D}(b) \tag{1}$$

where b is biomass density [ML^{-2}], $\mathbf{x} = (x, y)$ are spatial coordinates [L], t is time [T] and W is the plant available soil water [L_w].

$\mathcal{G}$ represents vegetation growth [$ML^{-2}\ T^{-1}$], $\mathcal{F}$ represents vegetation decay [$ML^{-2}\ T^{-1}$] and $\mathcal{D}$ represents the spatial propagation of vegetation [$ML^{-2}\ T^{-1}$], and they are defined in the original model as

$$\mathcal{G}(b,W) = c_b\,\mathcal{U}(b,W) \tag{2}$$

$$\mathcal{F}(b) = d_b b \tag{3}$$

$$\mathcal{D}(b) = D_b \nabla^2 b \tag{4}$$

Growth $\mathcal{G}$ is in turn is a function of the water uptake $\mathcal{U}$ rate [$L_w\ T^{-1}$], defined as

$$\mathcal{U}(b,W) = g_b \frac{W}{W + k_b} b \tag{5}$$

All parameters required for Eq. (1) are described in Table 1.

In the water-limited modelling context, soil water W [L] dynamics are also commonly represented by a reaction–diffusion PDE (e.g. Gilad

et al., 2007; HilleRisLambers et al., 2001; Rietkerk et al., 2002; Siteur et al., 2014a)

$$\frac{\partial W}{\partial t} = D_w \nabla^2 W + \mathcal{U} - i \tag{6}$$

Infiltration i [L T^{-1}] is modelled as depth-dependent and enhanced by the presence of biomass to represent the vegetation-infiltration feedback, as is common for these types of ecohydrological models (Gilad et al., 2007; Rietkerk et al., 2002).

$$i = \alpha h \frac{b + kW_0}{b + k} \tag{7}$$

All parameters are defined in Table 1. The spatial propagation of vegetation D is described in the original model proposed by HilleRisLambers et al. (2001) by means of linear diffusion, where D_b is a constant diffusion coefficient [L^2 T^{-1}]. We purposely choose to keep such formulation instead of incorporating seed dispersal terms (Eigentler and Sherratt, 2018; Pueyo et al., 2008; Saco et al., 2007; Thompson and Katul, 2009; Thompson et al., 2014). Although seed dispersal has been argued as relevant for controlling upstream band migration (UBM) rates, it introduces additional parameters which allow tuning UBM rates, with still unclear relation to the processes, including even downslope band migration Baartman et al. (2018). We prefer to keep vegetation propagation as simple as possible, since the goal in this study is to deepen the study of the hydrodynamic and hydrological aspects of banded VSO, instead of widening the breadth of processes.

We propose to represent surface hydrodynamics with the Zero-Inertia (ZI) – also often rather inaccurately called diffusive-wave – equation, a simplification of SWE (Caviedes-Voullième et al., 2018, 2020), but which allows to explicitly consider arbitrary topography.

2.1. Shallow water models for surface flow

The 2D shallow water equations, in conservation form are

$$\frac{\partial \mathbf{U}}{\partial t} + \nabla \Big[\mathbf{E}(\mathbf{U}) + \mathbf{G}(\mathbf{U}) \Big] = \mathbf{S}(\mathbf{U}) \tag{8}$$

where $\mathbf{U}$ is the vector of conserved variables

$$\mathbf{U} = \left[h, q_x, q_y \right]^\top \tag{9}$$

with water depth h [L] and unit-discharge (momentum) q_x and q_y in the x and y directions [L^2 T^{-1}]. Note that

$$q_x = hu \qquad q_y = hv \tag{10}$$

where $u = \mathbf{u}\mathbf{n}_x$ and $v = \mathbf{u}\mathbf{n}_y$, are the Cartesian components of the velocity vector $\mathbf{u}$ [L T^{-1}]. The fluxes in Eq. (8) are

$$\mathbf{E}(\mathbf{U}) = \left[q_x, \frac{q_x^2}{h} + \frac{gh^2}{2}, \frac{q_x q_y}{h} \right]^\top \tag{11}$$

$$\mathbf{G}(\mathbf{U}) = \left[q_y, \frac{q_x q_y}{h}, \frac{q_y^2}{h} + \frac{gh^2}{2} \right]^\top \tag{12}$$

where g is the acceleration of gravity [L T^{-2}]. The source term $\mathbf{S}(\mathbf{U})$ expands to

$$\mathbf{S}(\mathbf{U}) = \mathbf{B}(\mathbf{U}) + \mathbf{H}(\mathbf{U}) + \mathbf{I}(\mathbf{U}) + \mathbf{R} \tag{13}$$

where $\mathbf{B}(\mathbf{U})$ is the bed slope source term

$$\mathbf{B}(\mathbf{U}) = \left[0, -gh\frac{\partial z}{\partial x}, -gh\frac{\partial z}{\partial y} \right]^\top \tag{14}$$

and z is bed elevation [L]. $\mathbf{H}(\mathbf{U})$ is the friction source term

$$\mathbf{H}(\mathbf{U}) = \left[0, -gh\sigma_x, -gh\sigma_y \right]^\top \tag{15}$$

in terms of friction slopes σ_x and σ_y. For generality, at this point no specific friction model is introduced. The source term $\mathbf{I}(\mathbf{U})$ accounts for infiltration/exfiltration phenomena

$$\mathbf{I}(\mathbf{U}) = \left[i(\mathbf{U}), 0, 0 \right]^\top \tag{16}$$

where i is the infiltration rate if negative, or exfiltration rate if positive [L T^{-1}]. Note that conceptually, the infiltration rate depends on depth, but that dependency can be modelled with different levels of complexity. The rain source term $\mathbf{R}$ is simply defined in terms of the rain rate r [L T^{-1}].

$$\mathbf{R} = \left[r, 0, 0 \right]^\top \tag{17}$$

The numerical solution of (8) is complex and computationally demanding, which has lead to a number of simplifications, namely the Kinematic Wave (KW), the Zero-Inertia (ZI)—also often termed Diffusive Wave (DW), and the Local-Inertia (LI) approximations. All these approximations are based on simplifications of the momentum equation. Consider the momentum equation in the x-direction (the y-direction is analogous)

$$\overbrace{\frac{\partial q_x}{\partial t}}^{\mathcal{A}} + \overbrace{\frac{\partial}{\partial x}\left(\frac{gh^2}{2}\right)}^{\mathcal{B}} + \overbrace{\frac{\partial}{\partial x}\left(\frac{q_x^2}{h}\right)}^{\mathcal{C}} + \overbrace{\frac{\partial}{\partial y}\left(\frac{q_x q_y}{h}\right)}^{\mathcal{D}} = \overbrace{-gh\left(\frac{\partial z}{\partial x} + \sigma_x\right)}^{\mathcal{E}} \tag{18}$$

The LI form is obtained by neglecting the convective acceleration terms $\mathcal{C}$ and $\mathcal{D}$ (de Almeida and Bates, 2013). The LI form has not been reported in VSO literature and is not further discussed here.

The ZI form is obtained by additionally neglecting the local (temporal) acceleration term $\mathcal{A}$, making the momentum equation steady (Caviedes-Voullième et al., 2020). This leaves hydrostatic pressure gradients ($\mathcal{B}$) and gravity as drivers of flow, with friction ($\mathcal{E}$) opposing flow. Thus, the 2D momentum equation becomes

$$\nabla (h + z) = -\sigma \tag{19}$$

The KW form is obtained by also neglecting the hydrostatic term $\mathcal{B}$, and thus the only force driving flow is gravity, resulting in a momentum equation with the form

$$\nabla z = -\sigma \tag{20}$$

With both the ZI and the KW forms, the resulting momentum equations can be substituted back into the mass conservation equation, thus resulting in a single PDE to solve.

The applicability range and computational implications of these forms has been widely discussed in the literature (e.g. Caviedes-Voullième et al., 2018, 2020; Costabile et al., 2011; Cozzolino et al., 2019; Khosh Bin Ghomash et al., 2024; Tsai, 2003, and references within). For the purposes of the approach here, what is most relevant is that (i) both ZI and KW cannot accurately represent fast transients, since local acceleration $\mathcal{A}$ is neglected, and (ii) KW does not allow flow over rough horizontal beds, as is evident from (20). This latter KW limitation leads to select the ZI form henceforth, since it allows for more general topographies. We argue that the limitations of the ZI form in terms of fast transients are not critical for rainfall–runoff flows as those of interest here (Caviedes-Voullième et al., 2020), and thus it is a reasonable compromise in physical complexity.

2.1.1. Zero-inertia surface flow model

Eq. (19) can be expanded in terms of the unit discharge $\mathbf{q}$ [L^2 T^{-1}] directly in terms of the water surface slope $\mathbf{Z} = \nabla(h + z)$ [-] and paired with the mass conservation equation (Caviedes-Voullième et al., 2020)

$$\frac{\partial h}{\partial t} + \nabla \mathbf{q} = i \qquad \mathbf{q} = \theta(h)\frac{\mathbf{Z}}{\sqrt{|\mathbf{Z}|}} \tag{21}$$

where $\theta(h)$ is a non-linear coefficient which depends on the friction formulation of choice, to maintain generality (Santillana and Dawson, 2010). which is a function of the friction representation. Herein, we adopt the Darcy–Weisbach friction law

$$\theta(h) = h^{3/2}\left(\frac{8g}{f}\right)^{1/2} \tag{22}$$

where f [−] is the friction coefficient and g [LT^{-2}] the acceleration gravity.

2.2. Numerical implementation

The system defined by the biomass Eq. (1), the subsurface flow Eq. (6) and the surface flow Eqs. (21) and (22) is solved by a first-order accurate Finite Volumes scheme, with explicit time integration over a Cartesian structured mesh (Caviedes-Voullième et al., 2020). Because of the explicit time integration strategy, the numerical scheme is conditionally stable, and must satisfy

$$\Delta t \leq \min(\Delta t_b, \Delta t_w, \Delta t_h) \tag{23}$$

where Δt_b and Δt_W are the time step restrictions due to the stability of the biomass Eq. (1) and the subsurface flow Eq. (6) which follow formal linear diffusion stability

$$\Delta t_b \leq \frac{\delta x^2}{2D_b} \qquad \Delta t_w \leq \frac{\delta x^2}{2D_w} \tag{24}$$

Stability for the ZI surface flow Eq. (21) follows a relaxed Courant–Friedrichs–Lewy (CFL) condition, instead of a formal non-linear diffusion based stability, for efficiency reasons (Caviedes-Voullième et al., 2020; Cea et al., 2010; Dottori and Todini, 2011; Wang et al., 2011).

$$\Delta t_h \leq \mathrm{CFL}\frac{\delta x}{\max(q_\omega h_\omega^{-1})} \tag{25}$$

where q_ω is the surface water flux [L^2 T^{-1}] across a cell edge ω, and the coefficient CFL ≤ 1 to guarantee stability.

A consequence of the time-step constraint in Eq. (25) is that the stable time step size is variable in time, as it is dependent on flow conditions – and in turn on rainfall variability. As the flow becomes more complex, the time step size is reduced accordingly. This requirement, although carrying a computational cost, also ensures that surface flow is solved at a temporal resolution consistent to the temporal scales of the runoff process, especially relevant when considering intermittent rainfall (Crompton and Thompson, 2021). This has never been the case in VSO modelling, where solvers typically use a fixed time step in the scale of hours to days. Moreover, the full stability criteria (23) retains this property, as in the presence of surface flow usually Δt_h will be smallest. In the absence of surface flow the time step will adapt to the requirements of biomass and subsurface flow dynamics. These time steps (Eq. (24)) are not time dependent, but controlled solely by spatial resolution and diffusion coefficients. In this way, the numerical model natively allows a temporal multiscale solution which adapts to the scales of the processes occurring at any time, addressing a characteristic issue of banded system dynamics (Siteur et al., 2014a).

3. Study setup

The study consists of a sensitivity analysis over a four-dimensional parameter space: (i) topography profiles, (ii) average slopes, (iii) annual rainfall, (iv) rainfall frequency.

3.1. Domain, boundary and initial conditions

A set of hillslope surfaces were designed, all of which are topographic variations over the same domain. The computational domain $X \times Y = 300 \times 90$ m, was discretised with a spatial resolution of $\delta x = \delta y = 2$ m, resulting in 6750 square cells, as shown in 1(a). The surfaces always slope from left to right. Contrary to the most commonly used setup of periodic upslope–downslope boundary conditions, here we use *non-periodic boundaries* so that the downslope boundary (blue boundary in 1(a)) is set as a transmissive boundary, and all others are set as closed (reflective) boundaries. Initial conditions for vegetation were set so that 1% of the domain has vegetation cover. Initial biomass density in vegetated areas is identical, with $b(\mathbf{x}, t = 0) = 15$ gm^{-2}. All boundaries are transmissive to biomass fluxes, but no influx of biomass is prescribed, assuming there is no migration from regions downslope of the domain. Prescribing a biomass influx would require a guess of how much biomass migrates, or a spatially-fixed pool of biomass which would grow and migrate. Both of these ideas are quite poorly defined. We impose the simplest option of a null influx, as in previous studies with non-periodic boundaries (Baartman et al., 2018; Crompton et al., 2023; Saco et al., 2007).

The initial spatial distribution was randomly generated but was kept identical for all simulations. Initial surface water depth was set to $h(\mathbf{x}, t = 0) = 0$, and subsurface water was set to $W(\mathbf{x}, t = 0) = 3.75$ mm for all cases.

3.2. Surfaces

Three hillslope profiles were designed: linear (plane), concave and convex (Fig. 1(b)), described by

$$z_2(x - x_0)^2 + z_1(x - x_0) + z_0 \tag{26}$$

where x_0 is a reference position, z_0 is a reference elevation, z_1 represents the regional slope, and z_2 the curvature. Evidently $z_2 > 0$ corresponds to concave surfaces, $z_2 < 0$ to convex, and $z_2 = 0$ to linear planes.

Seven average (regional) slopes (z_1) were selected: 0.1%, 0.2%, 0.5%, 1.0%, 2.0%, 5.0% and 10%. In nature, slopes allowing for bands are mostly between 0.08–2.1 (Barbier et al., 2006; Deblauwe et al., 2008, 2011; Eddy et al., 1999; Galle et al., 1999; Pelletier et al., 2012; Tongway et al., 2001; Valentin et al., 1999), and exceptionally on steeper slopes (Bergkamp et al., 1999; Cammeraat and Imeson, 1999), while milder slopes transition into spotty patterns (Barbier et al., 2006).

All permutations were used, for a total of 21 different surfaces. The downstream elevation (right boundary) was always zero. The highest elevation of the hillslope varies with the slope. The surfaces were designed so that planes, convex and concave surfaces of the same regional (average) slope have the same upslope elevation. This means that average slope is the actual slope of linear planes, but is only the average (regional) slope in the case of convex and concave surfaces.

Fig. 1(b) shows profiles of the surfaces with an average slope of 0.5% (note the difference in axes scales). Our setup has some similarities to that of Baartman et al. (2018). However, they only studied surfaces with a regional slope of 1.4% and did not perform a systematic study of the interaction of different hillslope shapes and a range of average slopes.

3.3. Rainfall

We designed a simple rainfall signal as a set of periodic pulses, in contrast to the constant rainfall most often used in VSO literature. Pulse duration was set always to one day, after which a certain number of dry days occur, and a new identical event (single day pulse) happens. Rainfall intensity is constant during the event. A set of signals were generated from different annual rainfall and pulse frequencies. We selected pulse signals instead of fully stochastic rainfall signals for simplicity, as these pulses are easily and clearly characterised. Banded vegetation has been reported for mean annual rainfall in the range of 75–640 mm (Valentin et al., 1999), well within the well-established range of semi-arid and arid precipitation (Deblauwe et al., 2008, 2011; Meron et al., 2004). Following this, four total annual rainfall volumes were selected within such range (200 mm y^{-1},300 mm y^{-1},400 mm y^{-1},500 mm y^{-1}). Three different pulses-per-year were selected (40,60,100) representative of frequency for semi-arid climates (Guttal and Jayaprakash, 2007; Lázaro et al., 2001; Modarres and de Paulo Rodrigues da Silva, 2007; Panthou et al., 2018; Rodríguez-Caballero et al., 2018). This pseudo-steady pulsating rain with constant frequency repeats itself throughout the entire simulation. Table S1 in the Supplementary Information shows the resulting pulse intensities. Note that this rainfall design still neglects some features of rainfall in semi-arid and arid climates, such as seasonality (Vico et al., 2014), the distribution of many low intensity and very

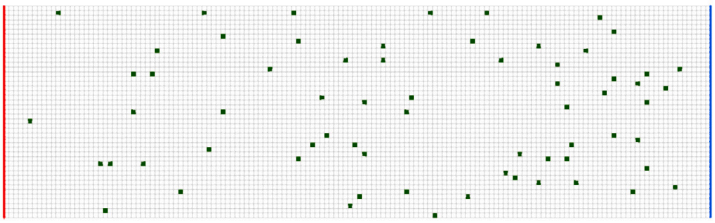

(a) Computational mesh, boundaries and initial conditions

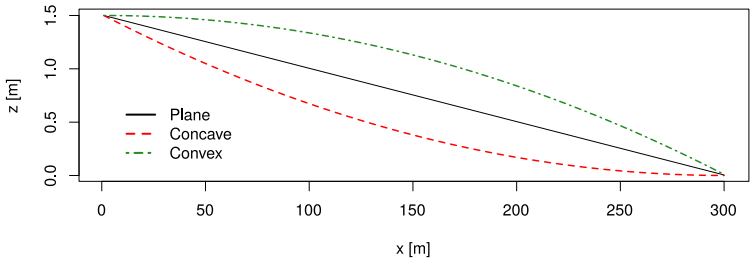

(b) Surface profiles, 0.5% regional slope

Fig. 1. Mesh and surface examples.

few large intensity rainfall events (Chamizo et al., 2012), and intra-storm intermittency (Dunkerley, 2018c,b). Although all these features have been noted to play roles in VSO, we intend to explore the role that capturing runoff process time scales can play in VSO. For this a simple intermittent signal suffices, as it allows for wetting and drying processes and easy interpretation. Of course, such features can be captured with fully stochastic rainfall signals. The analysis performed over the signal selected in this study can be extended to those additional features of the rainfall signal which imply secondary temporal scales coming from the forcing. This likely requires a more sophisticated analysis methodology. We leave this for future work.

3.4. Parametrisation

Table 1 shows the parameters selected for the biomass evolution model – Eq. (1) – and for the infiltration enhancement function — eq. (7). Most of the parameter values are taken following commonly used values, which are widely and consistently reported in the literature (e.g. Baartman et al., 2018; Baudena and Rietkerk, 2012; Caviedes-Voullième and Hinz, 2020; Dagbovie and Sherratt, 2014; Guttal and Jayaprakash, 2007; Pueyo et al., 2008, 2010; Rietkerk et al., 2002; Roitberg and Shoshany, 2017; Saco et al., 2007; Saco and Moreno de las Heras, 2013; Sun et al., 2010; Thompson and Katul, 2009). The exception are two of the values which shape the infiltration enhancement function Eq. (7). Most studies set $W_0 = 0.2$ and $\alpha = 0.2$. The exceptions are the works with non-periodic boundary conditions which use $W_0 = 0.05$, $\alpha = 8$ (Baartman et al., 2018) or $W_0 = 0.05$, $\alpha = 28$ (Saco et al., 2007). Saco and Moreno de las Heras (2013) reports the standard $W_0 = 0.2$ but fails to report the value of α. It is not a coincidence that the studies which allow a downslope runoff loss require a modified parametrisation of infiltration, since the water must infiltrate during its single runoff trajectory, as it is not recycled into the upslope boundary and does not have a second chance at infiltration, as also highlighted by Crompton and Thompson (2021). Therefore, clearly larger infiltration capacity is required for the same vegetation uptake and growth parameters. Our parametrisation follows the same reasoning. This is particularly relevant, as the infiltration enhancement is key to determining vegetation patch size (Svoray et al., 2021).

Table 1
Model parameters.

Description	Param.	Value	Units
Water–biomass conversion rate	c_b	10	g m^{-2} mm^{-1}
Maximum uptake per unit biomass	g_b	0.05	mm (g d m^2)
Half-saturation water-uptake constant	k_b	5	mm
Death rate coefficient	d_b	0.25	d^{-1}
Biomass diffusion rate	D_b	0.1	m^2 d^{-1}
Subsurface water diffusion coeff.	D_w	0.1	m^2 d^{-1}
Surface water diffusion coeff.	D_h	100	m^2 d^{-1}
Soil losses coeff.	p	0.2	d^{-1}
Half-saturation infiltration constant	k	5	g m^{-2}
Bare soil infiltration factor	W_0	0.001	–
Fully-vegetated infiltration coeff.	α	43.2	d^{-1}

In total, 252 setups were simulated and analysed. Simulation time was set to 30 years. For efficiency, an early-stop condition was implemented, stopping the simulation 20 days after vegetation disappears completely since results thereon are of no interest. The model was implemented in C, with OpenMP parallelisation. All simulations were run on 20 CPUs i7-6950X @ 3.00 GHz. The total simulation time for the study was around 17 days. Individual simulations lasted anywhere between a few minutes to 15 h, with an average CPU time of 1.65 h, with roughly 30% of the simulations requiring longer than the mean time.

3.5. Postprocessing and indicators

The simulations provide the temporal evolution of domain-wide hydrological and vegetation signatures, and the spatiotemporal evolution of the hydrodynamic and biomass fields. In order to quantitatively assess the combined effects of topography and rainfall properties, these results were post-processed into several indicators designed for such purpose.

Firstly, commonly reported band properties such as bandwidth ω [L], interband width σ [L] and band wavelength λ [L] are measured in the simulations. It is worth noting that some definitions may be imprecise – e.g., *"band separation"* might mean interband width or band wavelength – and the full set of indicators may be necessary to

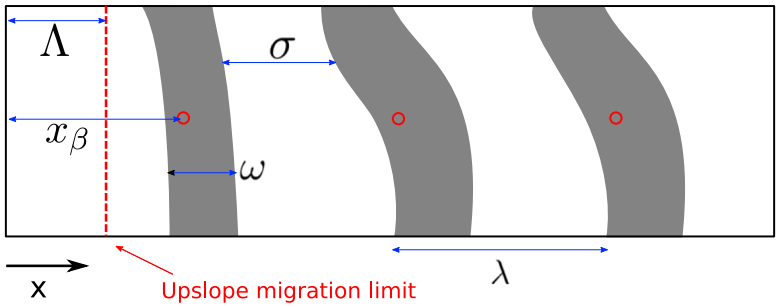

Fig. 2. Spatial descriptors of bands.

properly characterise the system (Gandhi et al., 2018). For example, both bandwidth reduction or increases in interband width can lead to reduced cover (Gowda et al., 2018). Fig. 2 defines spatial descriptors measured in the simulations. It must be noted that ω, σ, and λ may vary along the width of the domain (y-direction), and they may vary from one band to the next. We therefore summarise these quantities by computing the width-average by band (integrated along the y-direction) ω_β, σ_β, and λ_β, which are then averaged for all of the bands in the domain. That is, for ω

$$\omega_\beta(t) = \frac{1}{Y}\int_y \omega(y,t)\,dy \quad \forall x \in \beta \tag{27}$$

$$\bar{\omega}(t) = \frac{1}{N_\beta}\sum_{\beta=1}^{N_\beta}\omega_\beta(t) \tag{28}$$

where N_β is the number of bands β in the domain, and $\bar{\omega}$ is the averaged bandwidth indicator. $\bar{\sigma}$ and $\bar{\lambda}$ are obtained analogously. Note that these quantities remain time-dependent. The position of the centre-of-biomass of the leading (most upslope) band x_β [L] along the slope (x-direction) is computed following

$$x_\beta(t) = \iint_{A_\beta} x b(x,y,t)dx\,dy \left[\iint_{A_\beta} b(x,y,t)dx\,dy\right]^{-1} \tag{29}$$

where A_β denotes the surface covered by the band.

Based on the previous fundamental definitions, some additional indicators can be defined: the interband-width-to-bandwidth ratio $\rho(t) = \sigma(t)/\omega(t)$ (Valentin et al., 1999), which can also be averaged to obtain $\bar{\rho}(t)$.

Upslope band migration (UBM) is documented in field observations (Deblauwe et al., 2012; Hemming, 1965; Montaña, 1992; Montana et al., 2001; Tongway et al., 2001; Valentin et al., 1999) and strongly supported by theoretical and numerical results (Gilad et al., 2007; Klausmeier, 1999; Rietkerk et al., 2002; Sherratt, 2011, 2013; Thiery et al., 1995; Thompson and Katul, 2009; von Hardenberg et al., 2001). To quantify UVM, we define the band migration velocity v_β [LT^{-1}] as

$$v_\beta(t) = \frac{\partial x_\beta}{\partial t} \tag{30}$$

The upslope migration limit $\Lambda = \min(x_\beta)$ [L] is the x_β where the leading band stops migrating, i.e., when $\frac{\partial x_\beta}{\partial t} = 0$, and it is in fact the upslope-most x_β. It is a limit value and it is therefore not time-dependent.

A set of global, or domain-wide (integrated over the domain area A) indicators are also used. Total biomass B [M], total infiltration I [L^3], the total infiltration on vegetated areas I_b [L^3], and vegetation cover Ψ [-] are defined by

$$B(t) = \iint_A b(x,y,t)dx\,dy \tag{31}$$

$$I(t) = \iint_A i(x,y,t)dx\,dy \tag{32}$$

$$I_b(t) = \iint_{A_b} i(x,y,t)dx\,dy \tag{33}$$

$$\Psi(t) = A_b(t)A^{-1} \tag{34}$$

where A_b is the vegetated surface. We further define the infiltration ratio γ [−] as $\gamma(t) = I(t)(r(t)A)^{-1}$ and the vegetated infiltration ratio η [−] as $\eta = I_b(t)I(t)^{-1}$. Additionally, the life-span τ [T], defined as the time elapsed from the start of the simulation until vegetation entirely disappears from the domain . In a similar way, the τ_β [T] is defined as the elapsed time until the disappearance of the first leading band. This is a key time at which the system exhibits its most developed stage, as in most simulations steady states are not achieved.

4. Results and discussion

4.1. Spatiotemporal evolution example

In this section we present a detailed description of results for the cases computed with annual rainfall of 300 mm y^{-1}, distributed in 60 pulses, allowing for a full account of the process. Detailed results for other cases are omitted for brevity, but are analogous.

Fig. 3 shows the spatiotemporal evolution of biomass for selected surfaces. All three profiles and three slopes are presented to illustrate the different pattern evolution. The process is as follows. Vegetation evolves from the initial condition (Fig. 1(a)) as water becomes available. After 100 days (Fig. 3(a)) vegetation has begun to cluster in the downslope regions. The steeper slopes favour downslope clustering as there is where more water is available (clearly related to the larger upslope catchment area in this region). Mild-sloped plane and convex surfaces behave qualitatively the same, although for the steeper 1% slope, the convex surface shows a nearly bare domain with just a few surviving vegetation patches. Biomass in concave surfaces clusters strongly towards the downslope region, amplified by the low local slope favouring infiltration there. At t = 250d vegetation patches and incipient bands appear, and the relative behaviours amongst slopes and surfaces is similar as for earlier times. By t = 500d vegetation patches have mostly reshaped themselves into bands perpendicular to the slope. The downslope clusters of the concave surfaces have started to detach into bands which migrate upslope.

By t = 1500d bands are well established and migrating upslope in all surfaces. Characteristic band widths and bare soil distances separating them become obvious. The bands continue to migrate upslope up to a certain *upslope migration limit* Λ. Bands do not migrate further upslope from such position because the catchment area providing them water is not large enough to maintain them. As 3(d) shows, Λ shifts downslope (increases) with increasing average surface slope. For the same average slope, concave surfaces (∪) result in the most downslope (largest) Λ, followed by linear surfaces (\), and convex surfaces (∩) result in the upslope-most (smallest) Λ, i.e., $\Lambda_\cap < \Lambda_\backslash < \Lambda_\cup$. The figure also shows that the number of bands N_β and their geometrical properties are clearly different for each surface. The process continues with the leading band locking its position at Λ and then slowly decaying. The

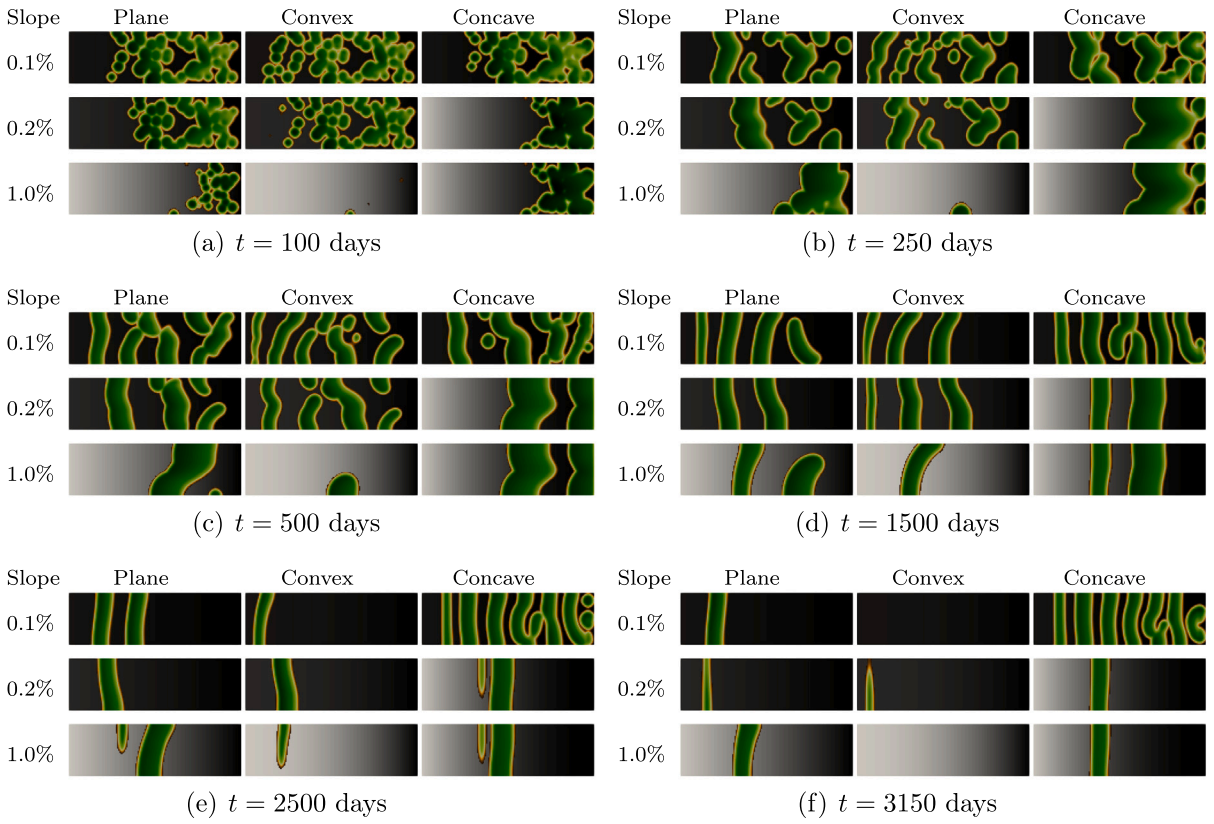

Fig. 3. Evolution of biomass distribution for $300\,\mathrm{mm\,y^{-1}}$ rain, 60 pulses per year, for selected surfaces and times.

fact that the band stops and decays implies that there is some unbalances in the vegetation dynamics. This is discussed in further detail in Section 4.1.1.

The decay of the leading band results in a lower infiltration, thus allowing for more runoff to reach the next band downslope. This second band therefore can harvest more water, grow stronger and then migrate upslope. As this new leading band disappears, the immediately downslope band repeats the same process as the previous band. As this continues, bands sequentially reach the same Λ as the first band and then decay. This happens at different rates for each surface, as can be seen in Figs. 3(e) and 3(f). Because the downslope boundary has no vegetation input, together with the absence of seed dispersal, total biomass in the domain decreases during the band migration and degradation, to the point that – in most simulations – vegetation disappears (before the 30 years of simulation) resulting in bare final states. It is relevant to highlight that the results shown here were computed with time steps $8 \leq \Delta t \leq 10000$s, with $\overline{\Delta t} \approx 6150$s overall, but $\overline{\Delta t} \approx 280$s during runoff, and $\overline{\Delta t} \approx 90$s during rainfall (Fig. S2 in the Supplementary Information) . This shows how temporal resolution adapts to the time scales of the processes, and vouches for the multiscale nature of the model. The temporal resolution achieved is far higher than for the classical Rietkerk solvers, which enforce constant time steps anywhere between 30 min (Rietkerk et al., 2002), daily time steps (Baartman et al., 2018) and annual time steps (Esteban and Fairén, 2006). Moreover, Figure S1 in the Supplementary Information illustrates the evolution of runoff during the simulation, which can be resolved thanks to the multiscale nature of the model.

4.1.1. Band slowdown and decay

For a band to be stable, the propagation, growth and decay rates must balance each other. The fact that the lead band decays implies that such balance is missing. This means that the position at which the band has stopped moving – the upstream migration limit – is not an equilibrium position for the band, just the position at which migration is no longer possible with the upstream water supply. As biomass is being lost from the band by attempting to propagate both upslope and downslope into the bare regions, the total loss remains larger than the growth, thus destabilising the band into a gradual death. Moreover, most of the infiltration occurs at the leading edge of the band, favouring a net biomass transfer from the core of the band into the upslope edge, where it simply dies off, because although it is wetter there, it is not wet enough. In contrast, while the band migrates, this leading edge progressively becomes the core of the band. This suggests that the model lacks some stabilising mechanism.

One way to view this is that the decay term $\mathcal{F}$ is too simplistic. Under constant rainfall, $\mathcal{G} > 0$ for $b > 0$. Under intermittent rainfall $\mathcal{G}$ may be zero even for $b > 0$ when $W = 0$. Therefore, the dynamics are only dependent on the simplified propagation and decay dynamics and their parameters. In nature, vegetation does not immediately start to decay after a few days without rain, especially for species well-adapted to water scarcity. It is arguable that vegetation initially would favour survival over reproduction, therefore biomass should not be invested into propagation. Additionally, the decay process requires a lag, as vegetation has a water store which must be depleted before actually decaying. Combined, these two behaviours would reduce the biomass sink, allowing for the band to better survive until the next rainfall.

Seed propagation (complementary to or replacing diffusive propagation) has been invoked as a stabilising mechanism, by imposing downslope (Saco et al., 2007) or anisotropic hydrochoric seed transport (Thompson and Katul, 2009). These approaches require tuning of at least two parameters, which, depending on parameter values, allow even for downslope band migration (Baartman et al., 2018). Although seed dispersal may resolve this inherent instability and is a plausible stabilising mechanism, other processes may be invoked. Our results

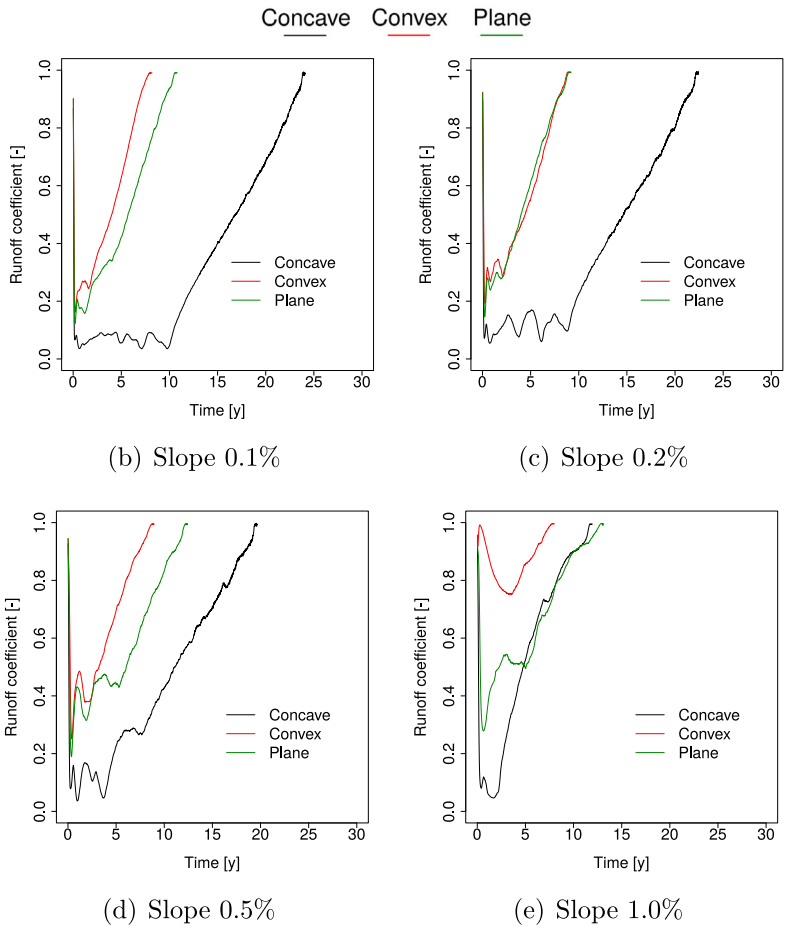

Fig. 4. Runoff coefficient evolution for $300\,\mathrm{mm\,y^{-1}}$ annual rainfall and 60 pulses per year for selected average slopes.

highlight that (in absence of anisotropic hydrochoric seed propagation) a stabilising mechanism may be necessary in the vegetation decay term, or also in the infiltration feedback formulation, as the system remains unstable in the absence of periodic boundaries and constant rainfall.

Other potential stabilising mechanisms may be found in the impact of microtopography on water redistribution (Dunkerley, 1997; Dunkerley and Brown, 1999; Eddy et al., 1999; Pelletier et al., 2012; Valentin and d'Herbès, 1999) and also on sediment redistribution, impacting VSO both via changing soil properties and topography (Pelletier et al., 2012; Saco et al., 2007; Saco and Moreno de las Heras, 2013). These approaches require to increase complexity further by introducing sediment transport equations and erosion/deposition, or landform evolution models. Similarly, other structural heterogeneities may induce stabilising (and destabilising) effects (Kästner et al., 2024, 2025).

We highlight that the standard approach in VSO literature uses periodic boundary conditions (e.g., Gilad et al., 2007; Dagbovie and Sherratt, 2014; Esteban and Fairén, 2006; Pelletier et al., 2012; Sherratt, 2016; Stewart et al., 2014, and many others, see Section 1). That implies that there is no geometrically defined area upstream of the upstream-most band, as the downstream runoff is recycled into such upstream area. Therefore, the phenomena discussed here cannot occur. In this sense, the idealised conditions of constant rainfall and periodic boundaries seem to act as an a-priori and artificial stabilising mechanism.

Herein we do not investigate the possible stabilising mechanisms (and propose this as follow up work), as we intend to keep the focus on the topography, rainfall variability and hydrodynamics in this context of net downstream loss.

4.2. Runoff

Fig. 4 shows the evolution of the runoff coefficient (of each rainfall event) for selected cases. This evolution provides some relevant insights. Firstly, towards the end of the simulations, when vegetation has disappeared, the runoff coefficient goes to unity, signalling that very little water remains in the hillslope under bare soil conditions. This can be seen to be a progressive (rather linear) evolution. More importantly, the runoff coefficient is non-zero during the entire simulation time, showing that there is always some runoff "loss" from the hillslope. This of course conflicts with the commonly used periodic boundary approach, in which water is recycled and therefore, in the end, the runoff coefficient is necessarily zero, i.e., all water infiltrates sooner or later. It can be seen though that during the most vegetated times of the banded system the runoff coefficients remain below 0.2. Fig. 4 also clearly shows how increasing slope accelerates reaching a runoff dominated hillslope. Although different behaviour of runoff coefficient evolution can be observed for different rainfall frequencies, no clear conclusion can be drawn. There is also no clear way of succinctly capturing a (time-independent) indicator of the evolution of the runoff coefficient, resulting from fundamentally transient banded systems, to evaluate its sensitivity to the environmental drivers studied here.

4.3. Spatiotemporal indicators

Fig. 5 shows biomass evolution for the same cases as Fig. 3 (rain $300\,\mathrm{mm\,y^{-1}}$, 60 pulses). Transparent colours in the figure show the full biomass signal – a noisy signal resulting from intermittency –, whilst solid lines are the trend of such signal. All cases shown in Fig. 5 result

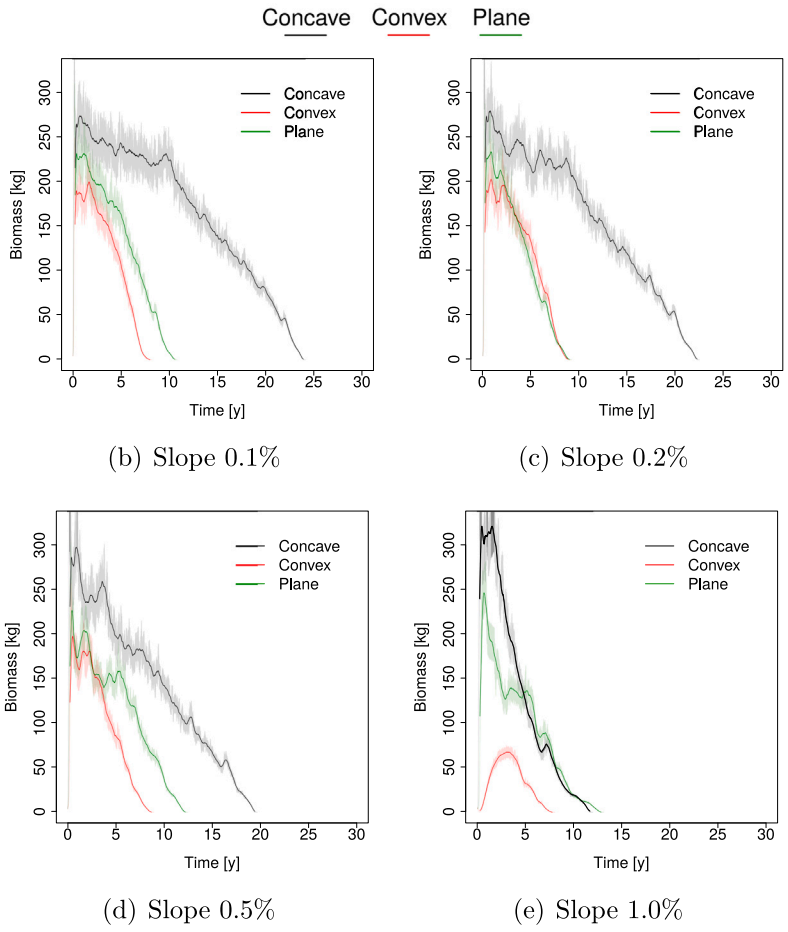

Fig. 5. Biomass evolution for $300\,\mathrm{mm\,y^{-1}}$ annual rainfall and 60 pulses per year for selected average slopes.

in bare states. The reason for this is the decay of the leading band which always stops migrating at the upslope migration limit, together with the lack of biomass input from downslope of the domain, as previously described. Biomass survives longer for concave surfaces (largest τ) and biomass temporal evolution is characteristically different for concave surface compared to both linear and convex surfaces. Life span τ appears inversely proportional to slope. As slope increases (e.g., 1%), convex surfaces are even less capable of supporting vegetation. The convex and linear surfaces show similar signals for a given slope, except for higher slopes in which the convex surface quickly fails to support vegetation. For this rainfall, higher slopes only support vegetation on concave surfaces.

Fig. 6 illustrates the band migration process, showing the temporal evolution of the position of the centre of biomass x_β for the leading (upslope-most) band. At early times ($t \leq 2\,\mathrm{y}$), x_β is always in the downstream half of the hillslope during the early vegetation clustering and band formation process. After the initial years, x_β moves upslope (decreasing x_β), initially at a high rate, but slowing down until it reaches the upslope migration limit Λ. Afterwards, a discontinuity appears, representing that the leading band has disappeared and now the next band immediately downslope becomes the leading band. This process is repeated a number of times until no bands are left, and x_β is reported as zero. The $\mathbf{x}_\beta(t)$ signal contains further information. Firstly, the number of well-developed migrating bands equals the number of discontinuities. Second, for a particular surface, all bands reach the same upslope limit $\mathbf{x}_\beta = \Lambda$, regardless of their position in the train-of-bands. Moreover, the position of the new-leading-band just after the leading band disappearance is always the same—i.e., the separation between the leading and second band (size of the discontinuity) is practically constant through time. A comparison across slopes shows that the upstream migration limit Λ is proportional to slope for all hillslope profiles, meaning that steeper slopes result in migration limits which are further downslope. The number of bands (number of discontinuities) is inversely proportional to slope for all profiles. The figure further quantitatively shows how the migration limit Λ follows the trend previously observed in Fig. 3 $\Lambda_\cap < \Lambda_\setminus < \Lambda_\cup$, and that $N_{\beta\cap} < N_{\beta\setminus} \leq N_{\beta\cup}$.

Fig. 7 shows upslope migration velocity v_β. There is an initial v_β peak occurring during the patch-clustering process (Fig. 3) corresponding to fast trajectory changes (Fig. 6). The initial and noisy velocity signal is meaningful, and only depicting how fast patches are clustering together into bands, but cannot be interpreted as band migration velocities. Once the signal stabilises, migration rates monotonically decrease to zero at the time when the leading band reaches the upstream limit. Similar to Fig. 6, a discontinuity in the migration velocity signal means that the leading band disappears, and a new leading band is now of interest. The v_β is maximised when the band becomes the leading band. The process is repeated for all bands. It is noteworthy that the v_β evolution is essentially the same for each band in the train-of-bands. Overall, Fig. 7 shows that peak and average migration velocity v_β is inversely proportional to slope. The hillslope profile results in the following trend $v_{\beta\cup} < v_{\beta\setminus} < v_{\beta\cap}$. Importantly, migration velocities for these cases are in the order of 20 $\mathrm{my^{-1}}$, far higher than reported field rates, up to 1.2 $\mathrm{my^{-1}}$ (Deblauwe et al., 2012; Gowda et al., 2018; Leprun, 1999; Valentin et al., 1999). The cause of fast rates is subject of discussion. UBM can be explained by the expansion–contraction dynamics of bands (Aguiar and Sala, 1999; Deblauwe et al., 2012; Gowda et al., 2018; Thiery et al., 1995), as a result of surface

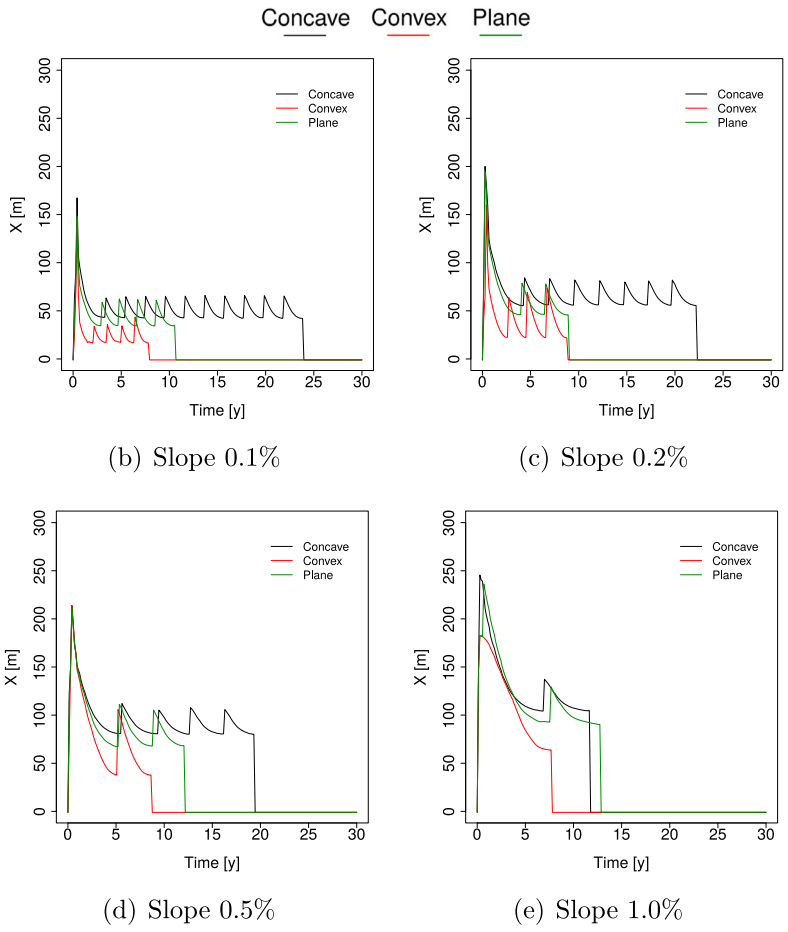

Fig. 6. Trajectory of the centre of mass of the leading band for 300 mm y^{-1} annual rainfall and 60 pulses per year for selected average slopes.

water-redistribution: upslope regions of the band receive more water than downslope regions of the band, thus, colonisation rates in the upslope direction are larger than in the downslope direction, resulting in UBM. Foti and Ramírez (2013), Ludwig et al. (2005), Paschalis et al. (2016). In consequence, migration velocity is dependent on both growth and decay rates in Eq. (1), and therefore their parametrisation can be partially responsible for the magnitude mismatch between our simulated UBM rates and the reported field observations. These results suggest that surface water redistribution itself – strongly coerced by topography – plays a role in determining the migration velocities. For example, for convex surfaces velocities can be up to twice as much as the velocities of concave surfaces, whereas migration rates for linear surfaces are somewhat slower than for concave surfaces. Since most of the computational modelling of these phenomena have been performed using linear advection models for surface flow which encode slope onto an advection coefficient and completely disregard topology, these effects have been historically overlooked. An obvious consequence of this is that band stabilisation may be achieved by factors affecting water velocities, such as topographic features, in particular microtopography or even topography co-evolution.

4.4. Sensitivity and trends

In this section we report and discuss a set indicators describing the response of the banded vegetation to all four dimensions of the parameter space, i.e., for all 252 simulations. A summary of trends is presented in Table 2. The indicators on the top panel have been frequently reported in field observations, whereas those in the lower panel are complementary analysis indicators. The trends reported in Table 2 are supported by figures for each indicator. Some trends are clearly proportional (↑) or inversely proportional (↓), whereas some are discernible but not robust (↗, ↘). A few trends are very strong and clear (⇑, ⇓), and some cases show no clear sensitivity or trend (⇝). Most of these trends are observed by comparing results of simulations just before the first band disappears $t \lesssim \tau_\beta$. Because no steady state is achieved in the process, this time has been selected as representative as the most developed condition of the system. A first general insight from Table 2 is that many indicators are sensitive, and sometimes quite strongly, to the hillslope profile. This means that real topographies must be accounted, in particular if meaningful parametrisation are to be calibrated through pattern-matching efforts. Otherwise, topographic effects are being lumped into parameters which – in principle – account for bio- and physiological properties, and not topographic properties. Concerning rainfall, there are some clear trends concerning the total rainfall. However, the trends on rainfall frequency are not as clear. Table 2 does show that there is a response of the pattern geometry to rainfall frequency, but the trends do not support more precise statements. This may point to issues with the rainfall design (i.e., frequency dominated), as Crompton and Thompson (2021) did find clear trends in the response to rainfall variability Similarly, the complex response of the pattern to the different drivers in Table 2 is consistent with the conclusions from Crompton and Thompson (2021) in that rainfall variability features alone do not determine the patterns.

A qualitative contextualisation of some of these indicators is provided in figures S7–S10 in the Supplementary Information. Such figures show the metrics computed from the simulations in this study, together with field data reported in the literature discussed in this section. We do not conduct a thorough quantitative comparison of these indicators, as we do not attempt to reproduce any specific field conditions.

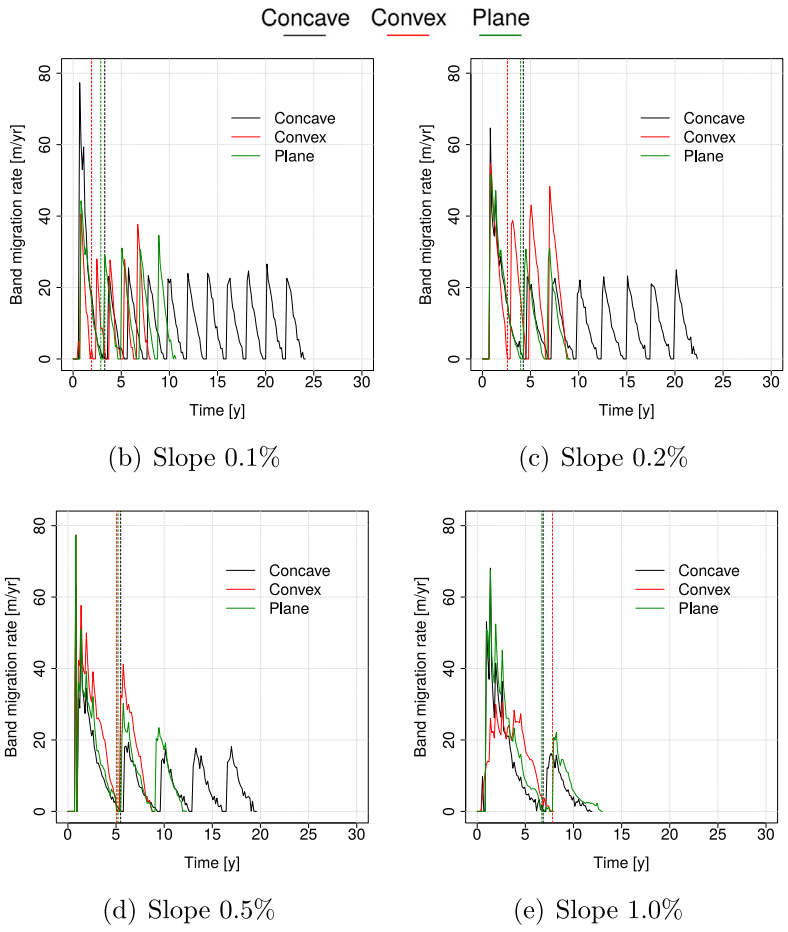

Fig. 7. Migration rate of leading band for 300 mm y^{-1} annual rainfall and 60 pulses per year for selected average slopes.

Table 2
Summary of trends and sensitivities.

Indicator	Symbol	Figure	Sensitivity to				Profile		
			Slope	Rainfall	Frequency	Profile	∩	\	∪
Mean wavelength	$\bar{\lambda}$	8	↓	↠	↠	+	+	~	−
Mean bandwidth	$\bar{\omega}$	9	↗	↑	↠	−	~	~	~ +
Mean interband width	$\bar{\sigma}$	10	↓	↓	↓	+	+	~	−
Interband:bandwidth ratio	ρ	11	↓	↓	↘	+	+	~	−
Migration rate	$\bar{v}_\beta$	12	↓ (↑)	↓ (↠)	↑	~	+	~	−
Upslope migration limit	Λ	13	⇑	↓	↑	+ −	~	+	
Number of bands	N_β	S4	⇓	↑	↑				
Life span	τ	S3	↓	↑	↗		−	~	+
First band decay	τ_β	S5	↑	↑					
Infiltration ratio	γ	15	↓	↗	↑	+	− ~	~	+
Vegetated inf. fraction	η	S6	⇓		↑		−	~	+

↗:= proportional to, ↘:= inversely proportional to, ↑:= strongly proportional to; ↓:= strongly inverse proportional to; − := smaller, ~:= medium, + := larger.

4.4.1. *Wavelength*

Wavelength (often imprecisely termed *separation*) is the most frequently reported geometrical indicator. Our results show an inverse relationship of wavelength to regional slope, consistently with reported observations (Deblauwe et al., 2011; Eddy et al., 1999; Pelletier et al., 2012; Penny et al., 2013; Valentin et al., 1999) and other simulations (Baartman et al., 2018; Sherratt, 2015). Fig. 8 shows wavelengths in the range of 25–125 m, within the range of observed wavelengths 25 – 250m (Deblauwe et al., 2012; Eddy et al., 1999; Gowda et al., 2018; Meron et al., 2004; Penny et al., 2013; Valentin and d'Herbès, 1999; Valentin et al., 1999). It is not surprising that the upper range of wavelengths is not reproduced by simulations, since the numerical results are constrained by the size of the computational domain. Importantly, Fig. 8 shows that wavelength can be sensitive to the hillslope profile, as was suggested by Baartman et al. (2018). Linear and concave hillslopes produce wavelengths inversely proportional to slope, consistently with field observations (Deblauwe et al., 2011; Eddy et al., 1999; Pelletier et al., 2012; Penny et al., 2013; Valentin et al., 1999), while the trend for convex surfaces is harder to read. Concave surfaces seem to exhibit shorter wavelengths than linear slopes, and convex surfaces show the largest wavelengths, qualitatively consistent with Baartman et al. (2018). Wavelength shows little sensitivity to annual rainfall, consistent with other modelling studies (Sherratt, 2013,

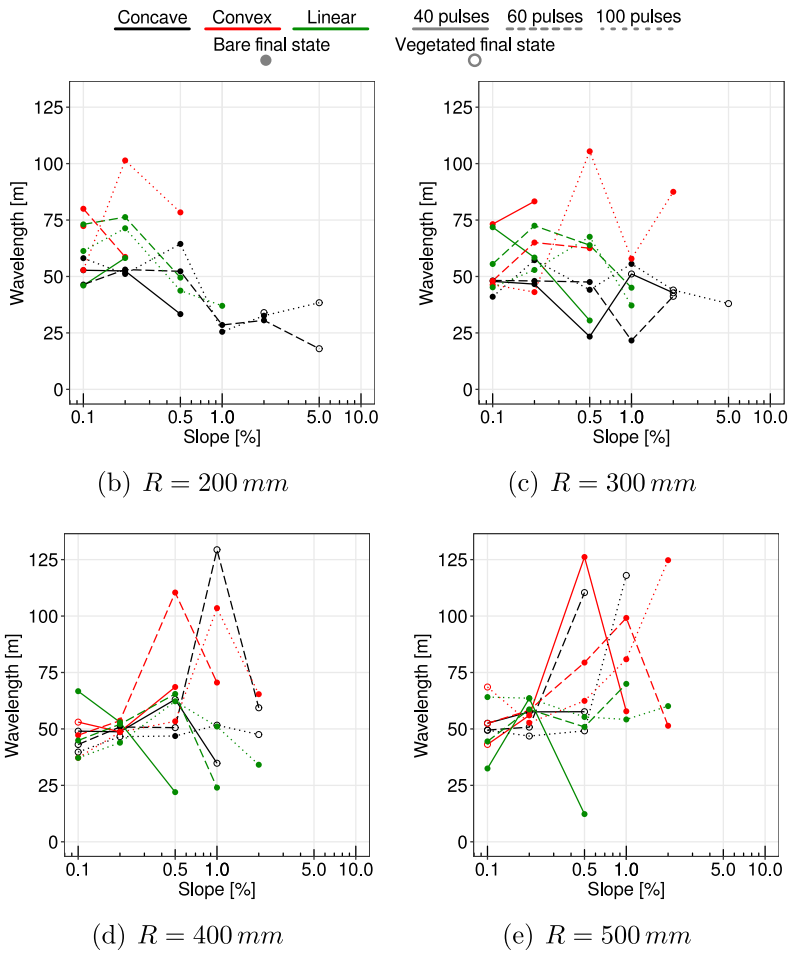

Fig. 8. Mean Wavelength $\bar{\lambda}$ results.

2015; Siteur et al., 2014b), although an inverse relationship has be reported from field observations (Couteron, 2002; Deblauwe et al., 2011, 2012; Gowda et al., 2018; Lefever and Lejeune, 1997; Lejeune et al., 2004; Valentin and d'Herbès, 1999). This discrepancy has been argued to be caused by temporal variability of rainfall (Sherratt, 2015; Siteur et al., 2014b). No clear trend is observed in response to rainfall frequency in our results, although other studies have found that shorter storms with higher precipitation result in larger wavelengths Crompton and Thompson (2021). However, we cannot fully assess this because of the design of our rainfall signals.

4.4.2. Bandwidth

Bandwidth $\bar{\omega}$ is shown (Fig. 9) to be positively related to slope, although weakly, and mostly on steep slopes. Field observations suggest inverse relationship, although they are only for slopes milder than 0.5% (Gowda et al., 2018; Valentin et al., 1999), making the comparison difficult. Bandwidth responds positively to total rainfall in the simulations, consistently with observations (Valentin et al., 1999). Rainfall frequency seems to be less relevant to determine bandwidth. There is a small sensitivity to hillslope shapes for $R \leq 300$ mm, although it increases with rainfall, in particular for concave surfaces. The simulated bandwidth is mostly between 10 – 100 m, but up to 200 m. This range is consistent, though wider, than the 10 – 50 m range in the literature (Fiorillo et al., 2017; Gowda et al., 2018; Moreno de las Heras et al., 2011, 2012; Valentin et al., 1999).

The higher bandwidth range occurs only for concave surfaces with either very steep slopes or high total rainfall. The reason for this is that such simulations result in single wide vegetated are (although not really a band) near the downslope boundary, where the slope is mildest.

4.4.3. Interband width

Interband width $\bar{\sigma}$ has been observed in the field to be inversely related to slope (Leprun, 1999; Pelletier et al., 2012; Valentin et al., 1999). The same trend is observed in the simulated results (except for convex surfaces, with no clear trend), especially for low rainfalls (see Fig. 10), as higher rainfall weakens the trend. Our results also show an inverse relation of interband width to annual rainfall, but reported observations are scarce to compare with. The range for interband spacing obtained from the simulations is 3.5–73 m, within the observed range in the field, of around 10–250 m (Deblauwe et al., 2012; Leprun, 1999; Moreno de las Heras et al., 2011, 2012; Valentin et al., 1999), although smaller values have also been reported (Pelletier et al., 2012). Interband width is negatively related to annual rainfall. Reported interband data are scarce to compare with. The results show hillslope shape has a strong effect on interband width. Concave slopes result in the shortest widths and convex slopes typically produce the largest interband widths. Our simulations confirm and extend results by Baartman et al. (2018) which hinted at variable interband width in non-linear hillslopes, although they did not perform a quantitative sensitivity assessment.

4.4.4. Interband:bandwidth ratio

The interband:bandwidth ratio ρ is often reported from field studies. The simulations show an inverse relation between ρ and slope – for concave and linear profiles –, consistent with observations (Gowda et al., 2018; Valentin et al., 1999; Valentin and d'Herbès, 1999) and other simulations (Sherratt, 2015). The trend may be an inverse exponential relation as previously suggested by Valentin and d'Herbès (1999). However, convex surfaces show a positive relation to slope,

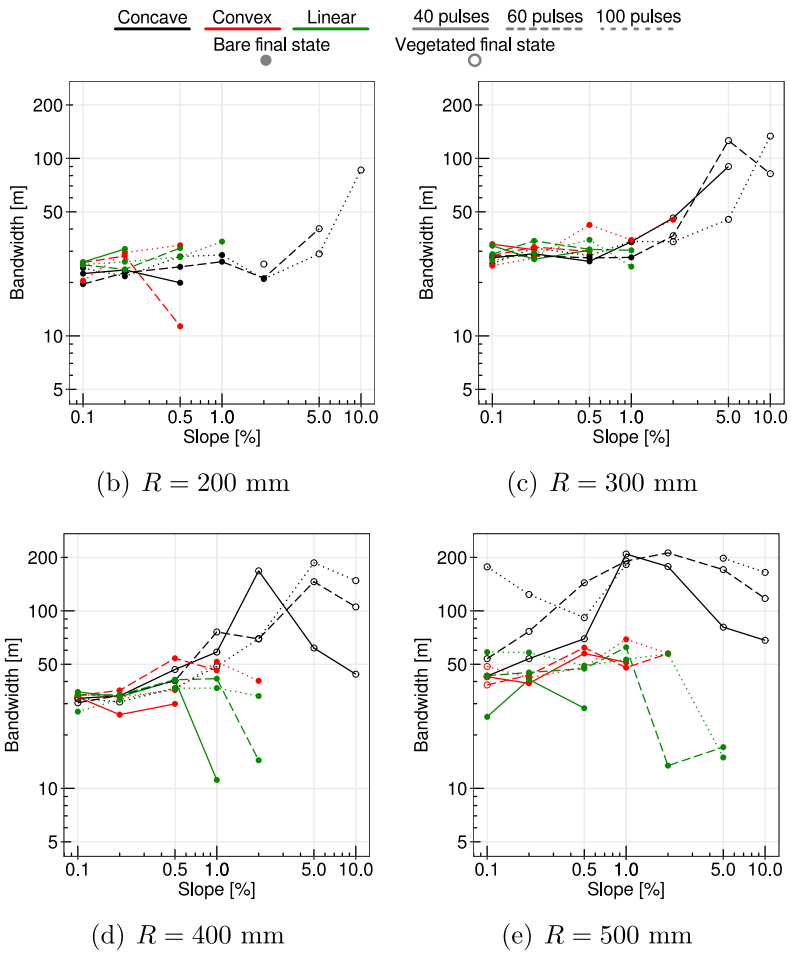

Fig. 9. Mean bandwidth $\bar{\omega}$ results.

consistent with the increase in interband width $\bar{\sigma}$ in Fig. 10. The ρ ratio is also inversely related to annual rainfall, consistent with observations by Valentin et al. (1999) who pointed out an inverse dependency of ρ to rainfall (see Figure S7 in Supplementary Information). The results also suggest a mild inverse dependency of ρ to frequency. As Fig. 11 shows, for most simulations $\rho \lesssim 2$. This is consistent with measured ranges around $0.51 \leq \rho \leq 2.3$ (Valentin et al., 1999) and $\rho \leq 3$ (Gowda et al., 2018). The hillslope profile has a strong effect on ρ, with smaller ratios obtained for concave surfaces, and the largest ratios mostly obtained for convex surfaces. It is interesting to highlight that the ρ ratio is sensitive to rainfall while wavelength is not, as first pointed out by Sherratt (2015). The results here show that both bandwidth (positively) and interband width (negatively) are sensitive to rainfall, so that their sum – i.e., wavelength – remains rather insensitive, but their ratio ρ is strongly inversely sensitive.

4.4.5. Band migration rate

Migration rates $\bar{v}_\beta$ are inversely related to slope in the case of concave and linear surfaces (although cases resulting in persisting systems show a weaker trend). This is consistent with reported field data (Deblauwe et al., 2012; Gowda et al., 2018). Convex slopes exhibit a different behaviour, in particular for higher rainfall. The difference may be explained by the nature of runoff. For concave and linear profiles, the migration rate is inversely related to rainfall, as also found by Sherratt (2011), but contradictory to results by Siteur et al. (2014b). Field data does not show a clear trend (Deblauwe et al., 2012; Valentin et al., 1999) Rainfall frequency has a positive effect on migration rates. As seen in Fig. 12, the range of simulated rates is 0.2–23.5 my^{-1}, similar to other model predictions (which go as high as 100 my^{-1}) year (Dagbovie and Sherratt, 2014; Gilad et al., 2007; Thompson and Katul, 2009), but far above those reported from observations (far) below 1.5 my^{-1} (Couteron et al., 2000; Deblauwe et al., 2012; Gowda et al., 2018; Leprun, 1999; Mabbutt and Fanning, 1987; Pelletier et al., 2012; Valentin et al., 1999).

The migration rate is also sensitive to the hillslope profile. Concave surfaces result in the slowest rates, linear slopes often result in faster migration rates and convex surfaces result in significantly faster rates. The sensitivity of migration rates to the profile might explain why contradictory conclusions may be found in reported trends, as the relatively small variations in topology can play a significant role. Furthermore, it has been proposed that migration rates should be sensitive to rainfall (as is in our results) but not to correlated to wavelength (Sherratt, 2011), although positive correlations to band wavelength have been reported (Deblauwe et al., 2012; Thompson and Katul, 2009). In all surfaces water depth is lower upstream, and increases in the downstream direction until bands, and infiltrating regions, are encountered. Higher depths also imply higher water velocity, which is therefore also increasing in the downstream direction. For linear surfaces, only the presence of bands changes this behaviour as the slope remains constant. In the case of concave surfaces, slope decreases in the downstream direction, thus possibly reducing velocity, although water depth may be increasing, which creates a competing influence. For convex surfaces however, the upstream region is one with low water depth and lower slope, therefore, clearly water velocity is lowest in the convex surface upstream regions. Slow moving water has higher chances of infiltrating, and therefore, increased water availability on the upslope band front is expected, which in turn favours band migration. The bands in concave surfaces also tend to be further upslope, because water availability is

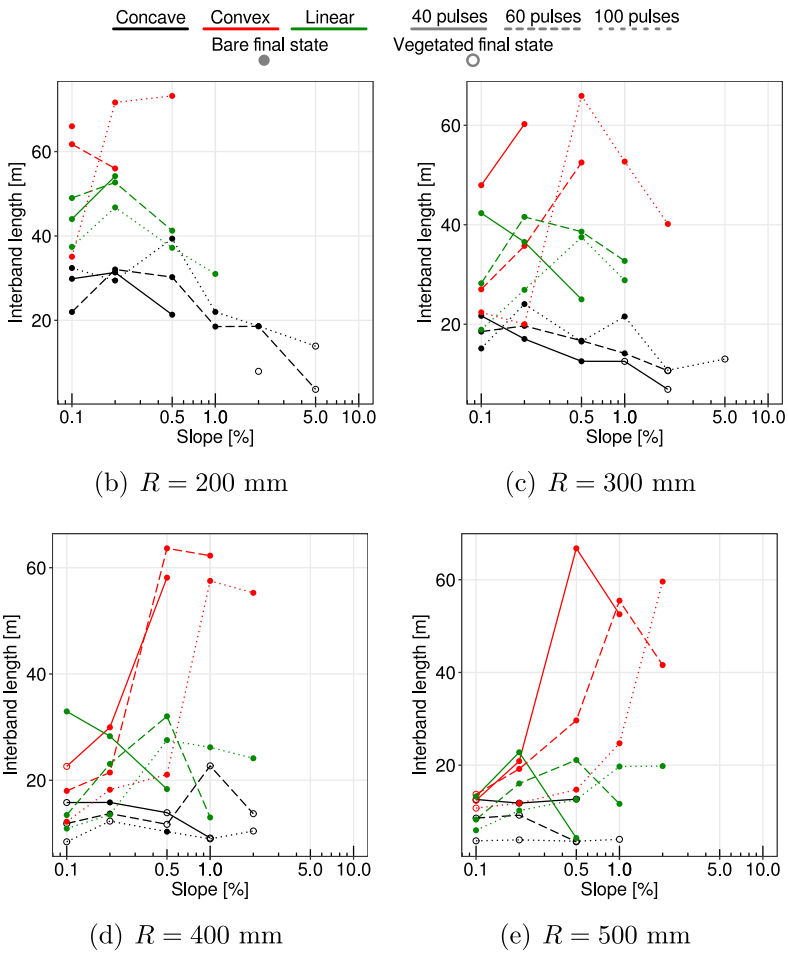

Fig. 10. Mean interband width $\bar{\sigma}$ results.

higher there due to the of the higher infiltration resulting from lower local slopes. This combined effect is likely responsible for the behaviour of migration rates and interband width in concave surfaces.

The clear mismatch between simulations and observations requires to understand which properties of the ecohydrosystem govern UBM rates (and migration itself) in nature. It remains unclear which mechanisms need to be included or improved in computational models to reproduce the observed rates (Dunkerley, 2018a). Our results highlight that hydrodynamic complexity caused by topography and rainfall variability can strongly modulate migration velocity. This is strongly related to the resulting complexity of the velocity field, as hinted by Consolo and Valenti (2019). In particular, less frequent rainfall tends to slow down band migration. This has been suggested to be strongly related to migration rates (Deblauwe et al., 2012; Dunkerley, 2002b), and also proposed as an UBM-inhibitor, through ephemeral ponding – and the subsequent evaporation – in the interband space leading to increased soil sealing and seed soaking injury (Dunkerley, 2018a; Pelletier et al., 2012), by controlling edaphic and pedological processes (Dunkerley, 2018a; Leprun, 1999), and also simply through rain-drought cycles (Dunkerley, 2018c). All of these secondary processes are of course also affected by hillslope shape and microtopography. Other mechanisms have been invoked to stabilise migrating bands, most notably through hydrochoric or non-local seed dispersal along the hillslope (Baartman et al., 2018; Consolo and Valenti, 2019; Eigentler and Sherratt, 2018, 2022; Saco et al., 2007; Thompson and Katul, 2009; Thompson et al., 2014), but also through soil erosion (Foti and Ramírez, 2013) and extended root systems (Couteron et al., 2000). Our results highlight that invoking additional processes – and additional parameters – may numerically stabilise bands, but not necessarily for the right reasons, or at least not in full. For example, Baartman et al. (2018), Consolo and Valenti (2019) found that, under certain parametrisations of downslope seed transport, even downslope migration is possible. Our results highlight that the hydrodynamics may already play some stabilising role. The reduced migration rates in response to infrequent rainfall suggest that the typical continuous rainfall approach in banded VSO modelling is also partially responsible for the migration rate mismatch. It is arguable that the combined effect of topography and rainfall with other possible stabilising mechanisms must be revisited, in particular those considering hydrochoric transport which are strongly affected by local velocities (Thompson and Katul, 2009). Moreover, the velocity of water flows might also influence defects in the bands (Pinto-Ramos et al., 2023). This all highlights the relevance of correctly simulating the hydrodynamics.

4.4.6. *Upslope migration limit*

The upslope migration limit Λ is not reported in the literature. However, it is an interesting property of the system, in particular because it is robust and time-independent. As summarised in Table 2 and shown in Fig. 13, Λ is positively related to slope, i.e., higher regional slopes force vegetation to develop further downstream, since higher slope favours runoff over infiltration. There is also a clear and systematic trend for all three hillslope profiles. Convex surfaces result in the upslope-most limits, followed by linear surfaces, followed by concave surfaces. This holds across the rainfall gradient, slopes and rainfall frequencies. Furthermore, higher rainfall frequencies result in migration limits further upslope. This is related to rainfall intensity. Since the same annual rainfall must be distributed with different frequencies, the result is that higher intensities (lower frequencies) favour

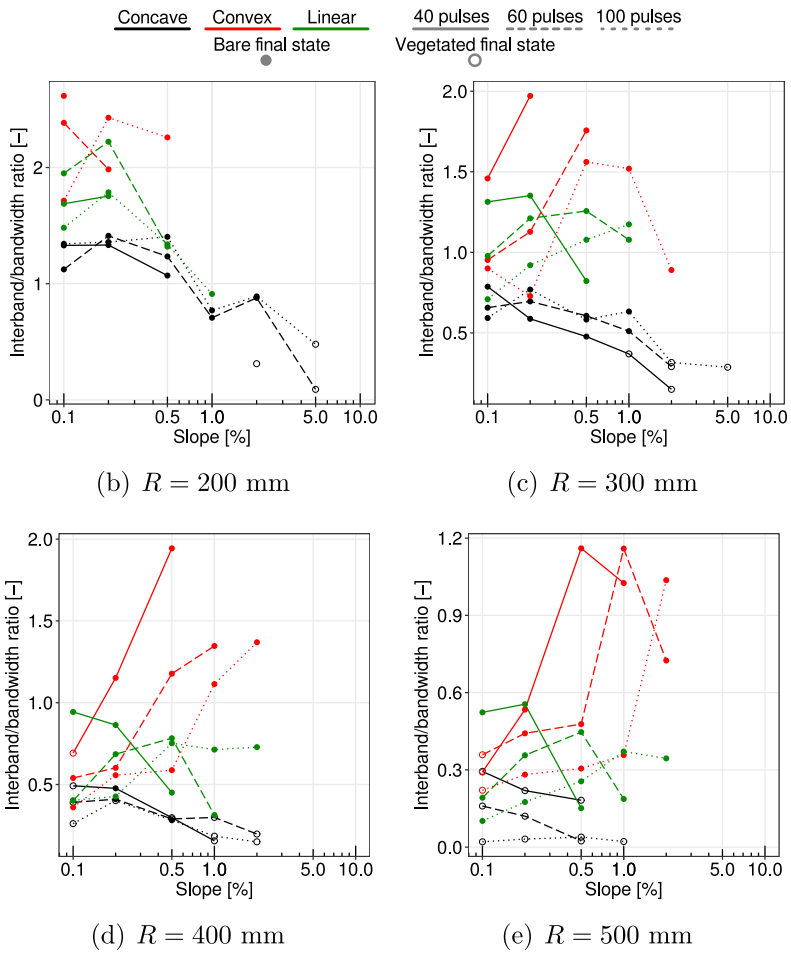

Fig. 11. Interband-bandwidth ratio ρ results.

runoff over infiltration, which manifests in a vegetation band requiring a larger bare soil upstream source area to collect enough water to achieve sufficient infiltration.

From a hydrological processes point-of-view, the upslope limit and the interband width should be related. Interband width must allow for a bare area to generate enough runoff to sustain a band. An optimal bandwidth and interband width are those that allow for all water from an upslope interband area to be captured by a band, and that no runoff exists immediately downslope of the band. With the same argument, under a linear slope, the interband width should be constant along the hillslope, and consequently equal to the distance between the top of the hillslope and the first band, i.e. the upslope limit. Fig. 14 shows this relation, categorised by each hillslope profile (together with linear fits) for all simulations. The figure shows that Λ is not a good predictor of interband width σ ($r^2 = 1.310^{-5}$) on concave surface, but positive trends exist for linear and convex surfaces ($r^2 = 0.265$ and $r^2 = 0.582$ respectively). Linear and concave surfaces result in upslope limit larger than interband width $\Lambda > \sigma$ (with slopes for the linear fits of 0.29 and −0.0006 respectively) which shows that optimal bandwidth and interband widths are not achieved. Hydrologically, this conveys that runoff from one interband space onto the other exists, implying a high runoff connectivity, i.e., a leaky landscape (Ludwig et al., 2007; Mayor et al., 2008; Okin et al., 2015; Saco et al., 2020). We highlight that this leakiness has controls both from the topography and the rainfall. Convex surfaces show $\Lambda < \sigma$ (linear fit slope of 1.2) which suggests that the geometrical arrangement is closer to optimal. This is difficult to explain hydrologically from a global budget point-of-view, and implies that the spatial distribution of the bands, in response to the variable local slope is playing a relevant role. Interestingly, although convex and linear slopes exhibit similar hydrological behaviour (e.g., runoff coefficients), the spatial metrics of the banded pattern (e.g., interband:bandwidth ratio, migration rate) are not closely related, whereas the correlation linear and concave surfaces is weaker hydrologically (Fig. 4, but somewhat stronger in terms of the spatial metrics (Fig. 11) and migration rates (Fig. 12).

The infiltration-rain ratio γ (or infiltration coefficient, and a complement of the runoff coefficient) shows an inverse relation to slope, as steeper surfaces favour runoff over infiltration. The ratio is positively related to rainfall frequency, since the rainfall design implies that higher frequency has lower intensity, which favours infiltration over runoff. A mild positive trend with annual rainfall is observed. There is a clear response of the infiltration-rain ratio to the different profiles. Concave surfaces favour infiltration. Convex surface seem to favour runoff more than linear surfaces. A very important feature of γ, is that it is not 100%, meaning that there is net runoff flowing out of the domain, and that such runoff is clearly dependent on slope, profile and rainfall properties (see Fig. 15).

4.4.7. Additional indicators

A number of indicators shown in Table 2 (which are not reported in the literature) are not discussed here for brevity. We refer to Supplementary Information for details.

The simulated life spans (Figure S3 in Supplementary Information) show an inverse relation to slope and positive to both rainfall and frequency, as well as a sensitivity to the hillslope profile. Although not exactly the same, rainfall variability has been negatively related to the resilience of vegetation patterns (Cueto-Felgueroso et al., 2015)

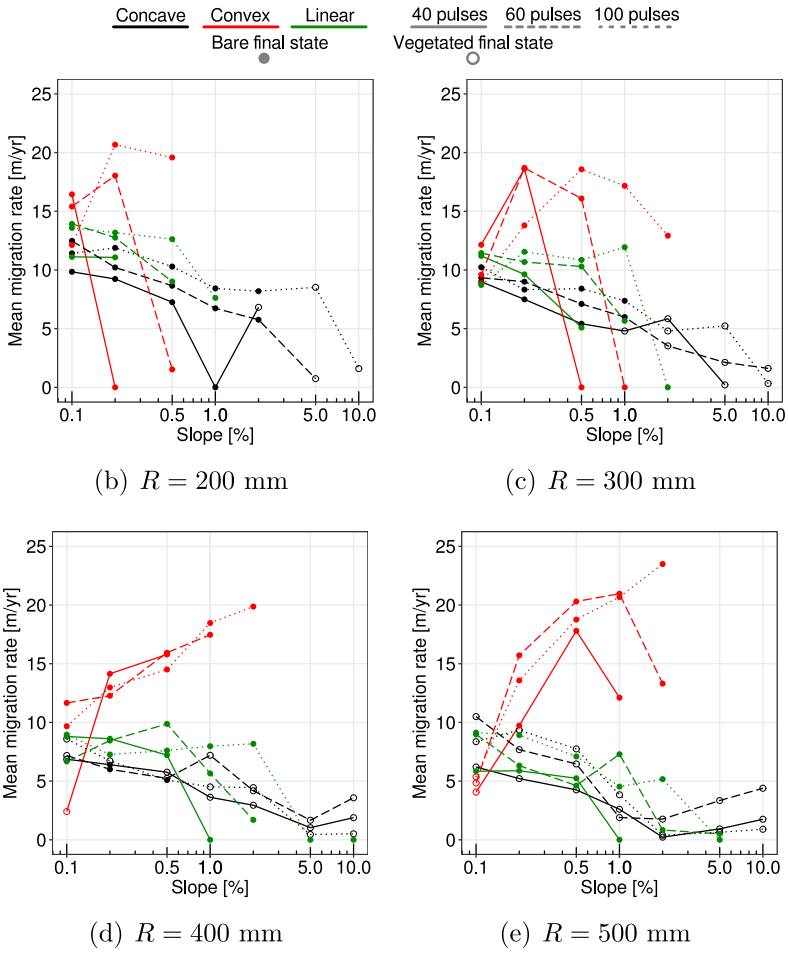

Fig. 12. Average migration rate of bands $\bar{v}_\beta$.

The number of bands obtained shows a very strong inverse relation to slope, a positive relation to frequency and clear sensitivity to the shape of the hillslope.

The time required for the first to disappear is positively related to slope and inversely o frequency. It shows little sensitivity to annual rainfall, but large sensitivity to the profiles.

5. Conclusions and outlook

The proposed ecohydrological model, based on the model by Rietkerk et al. (2002) and enhanced by the Zero-Inertia approximation to the shallow-water equations for surface flow was used to simulate vegetation band dynamics over 21 hillslope surfaces with different shapes and slope, and for 12 different rainfall signals.

The results allow for the following conclusions and insights. (i) The hillslope profile can have a very strong effect on vegetation band formation and dynamics. Significant differences appear in pattern geometry, migration velocity and hydrological behaviour, despite the small differences – arguably indistinguishable to an observer – in topography. This suggests that a large part of the pattern variability observed in the field may be explained by topographic features which have been neglected by only considering average regional slopes. Linear and convex hillslopes show similar behaviours, whereas concave surfaces behave characteristically differently. Consequently, DEMs with higher resolution – both horizontally and vertically – are necessary (Gandhi et al., 2018) to capture the hillslope shape under the mild slopes (below 2%) on which vegetation bands typically exist. The required resolution is currently technically possible (Bangen et al., 2014; Cucchiaro et al., 2019; Vericat et al., 2014), but far higher that the freely-available global DEMs (Moudrý et al., 2018) which may be the only ones covering banded vegetation regions. (ii) Intra-annual rainfall variability plays a role in wavelength selection, pattern properties and dynamics. In general, less frequent and more intense rainfall results in vegetation reaching further upslope, with larger interband spacing, and longer life spans. The results further show that the sensitivity of the ecohydrosytem to intra-annual rainfall distribution is dependent on both the topography and the annual rainfall (aridity) (Deblauwe et al., 2011; Djebou et al., 2015). This is the consequence of rainfall properties affecting infiltration and soil moisture patterns (Siteur et al., 2014a). (iii) General trends can be observed in response to the regional slope. Steeper slopes produce less bands, which are further apart, migrating at slower speeds, and upslope migration limits which are further downslope. A slope threshold exists above which bands cannot develop and establish, which is consistent with the literature. However, this threshold depends on the hillslope shape and to some extent on rainfall properties. (iv) The simulated upslope band migration rates is partially controlled by surface water velocity, and thus can be strongly affected (factor of 2) by hillslope profiles and rainfall variability, and remain still too fast compared to observations. This suggest that modelling additional features and process – e.g., seed dispersal (Saco et al., 2007; Thompson and Katul, 2009; Pueyo et al., 2010), microtopography (McGrath et al., 2012; Saco and Moreno de las Heras, 2013), bare soil compaction (Dunkerley, 2002a) – without considering the effects of topography and rainfall variability will likely result in parametrisations which may be right for the wrong reasons, embedding processes into model parameters (Deblauwe et al., 2012; Gowda et al., 2018; Penny et al., 2013; Ursino, 2005), and arguably only fitting converged states and not transients (Fatichi et al., 2016; Caviedes-Voullième and Hinz,

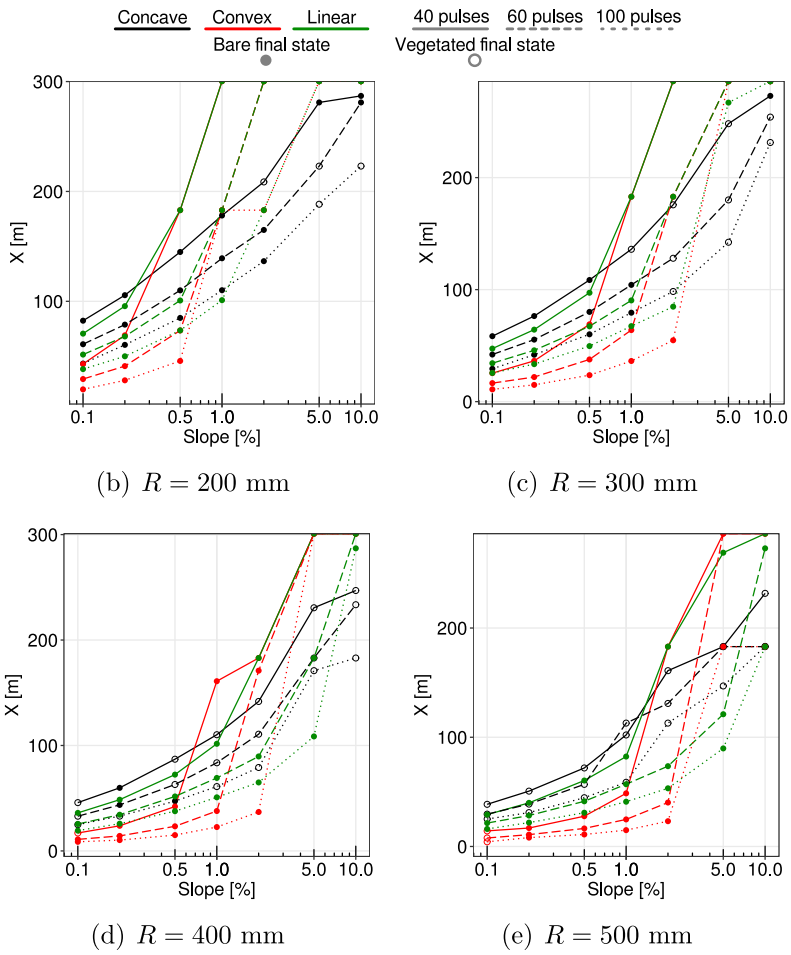

Fig. 13. Sensitivity of upslope migration limit Λ to all studied parameters.

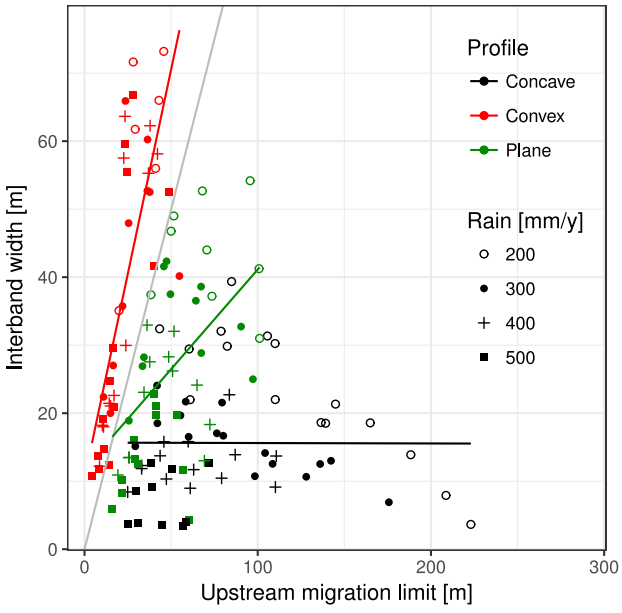

Fig. 14. Correlation between upstream migration limit and interband width.

2020). This is further related to the use of realistic non-periodic boundary conditions and thus accounting for net runoff losses, leading a re-parametrisation of the infiltration contrast (Baartman et al., 2018; Saco et al., 2007) which is essential for patterning (Foti and Ramírez, 2013). This in turn may be related to the use of simplistic depth-dependent infiltration instead of infiltration models accounting for soil water content (e.g. Green-Ampt), even through time-dependent proxy infiltration models (e.g., Horton) (Thompson et al., 2011). However, using these models is unlikely to result in infiltration differences of the magnitude observed with the infiltration contrast parameter (Caviedes-Voullième et al., 2021; Fernández-Pato et al., 2016).

The range of vegetation band dynamics is the result of hydrodynamic complexity of surface runoff arising from combinations of hillslope shapes and rainfall variability. Capturing these hydrodynamics is therefore essential to pursue transient simulations which can capture not only the resulting overall qualitative patterns but also band geometries and the rates (growth, decay, migration), both of which can be controlled by topography and rainfall properties. Topography and rainfall variability not only control local features within the system, but they strongly influence its connectivity and leakiness, thus strongly controlling the total water budget for the system (Khosh Bin Ghomash et al., 2019; Saco et al., 2020), and it interacts with the effects of vegetation on this hydrological partitioning (Farguell et al., 2022; Moreno de las Heras et al., 2020). This shows that highly resolved, multiscale, physically-based, and computationally efficient hydraulic models – such as the one proposed here – are required. Our results also highlight the need for quantitative indicators for patterns and band geometry, for which high resolution aerial and satellite photography is required, which is concurrent with other recent works (Caviedes-Voullième and Hinz, 2020; Gandhi et al., 2018; Gowda et al., 2018; Mander et al., 2017; Roitberg and Shoshany, 2017). This information is becoming increasingly accessible (Axelsson and Hanan, 2017; Fiorillo

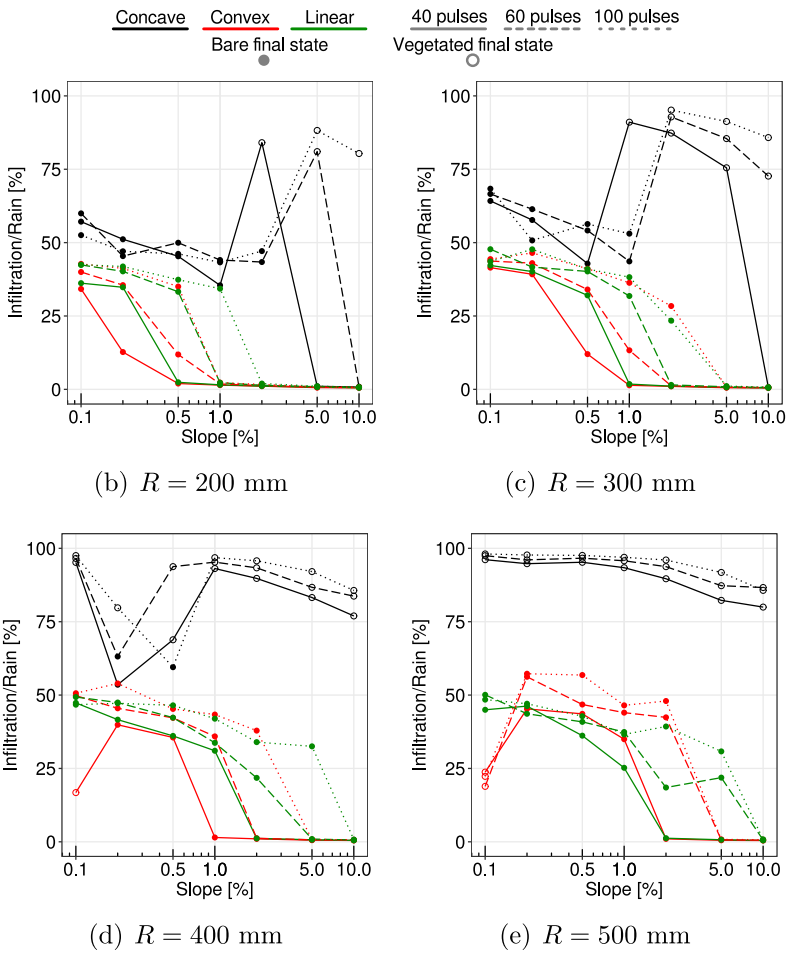

Fig. 15. Infiltration/rain ratio γ results.

et al., 2017), paving the way for better model evaluation and possibly model parametrisation. Having sufficient resolution and processes in a multiscale model, and comparing to quantitative spatial data of the patterns may also provide guidelines on how to address observational time scales in Ecohydrology (Estes et al., 2018). We must acknowledge that a limitation of this study is that we do not pursue a quantitative comparison with field observations mostly because of the unavailability of data to properly parametrise the model and expect a quantitative match. Nevertheless, since both the Rietkerk model and the ZI model have been validated against observations, it stands to reason that the simulations are physically plausible.

There are of course further system behaviours to be explored in response to additional sources of complexity within a multiscale modelling approach as the one presented here. Concerning rainfall, stochastic rainfall signals, annual variations in rainfall (Trichon et al., 2018), and the effects of successive small pulses or singular large pulses (Eddy et al., 1999) remain to be assessed systematically. In terms of topography, microtopography has been noted to play a significant role in VSO (McGrath et al., 2012; Saco et al., 2007), but the relationships between different topographic scales, namely microtopography vs hillslope scale (Caviedes-Voullième et al., 2021) remains to be explored in this context. It is also relevant to study the intertwined effects of the features explored here and their results of migration rates, together with previously proposed band stabilisation mechanisms (Baartman et al., 2018; Couteron et al., 2000; Eigentler and Sherratt, 2018; Foti and Ramírez, 2013; Pueyo et al., 2008; Saco et al., 2007; Thompson and Katul, 2009; Thompson et al., 2014). Additionally, exploiting the spatial and temporal resolution of simulations, it becomes possible to study the runoff-runon process, for example by assessing the water-harvesting efficiency (Esteban and Fairén, 2006; Valentin et al., 1999) of bands, and relating this to environmental properties of the system, and the geometry of the bands. These ideas together may allow further insights into the significance of processes, their representation in the models and their parametrisations. This would be a step further into evaluating the role that the dominant processes in VSO, and in particular topography-vegetation-hydrology interactions have in the broader Ecohydrology (Gutiérrez-Jurado et al., 2013), in particular considering that dryland dynamics may intensify and become more extended due to climate change (Grünzweig et al., 2022). This does not only imply a shift towards increased aridity, but to intensified rainfall variability and increase the relevance of runoff and runoff connectivity (Groner et al., 2023) which modulate resource availability, thus highlighting the relevance of the modelling approach taken here.

Finally, as an outlook, there is an ongoing effort to cast models such as the one presented here into high-performance computing frameworks, which will offset the computational costs and allow to scale-up simulations into catchment and landscape scales, maintaining high resolution – in particular, (Caviedes-Voullième et al., 2023) – while maintaining sufficient hydrological variability and hydrodynamic complexity, leveraging on increasingly available DEM and rainfall products. This will further strengthen the approach in terms of multiscale models, which appear essential to move forward (Crompton and Thompson, 2021). With such technology, it will be possible to test many of the potential stabilising mechanisms, add or improve additional processes such as erosion and sediment transport, resolve microtopography, better capture connectivity features and enrich the exploration of scale-dependent response of ecohydrological processes such as self-organisation integrally (Groner et al., 2023).

CRediT authorship contribution statement

Daniel Caviedes-Voullième: Writing – review & editing, Writing – original draft, Visualization, Validation, Software, Methodology, Investigation, Formal analysis, Conceptualization. **Yolanda Pueyo:** Writing – review & editing, Conceptualization. **Christoph Hinz:** Writing – review & editing, Writing – original draft, Supervision, Methodology, Conceptualization.

Declaration of competing interest

The authors declare that they have no known competing financial interests or personal relationships that could have appeared to influence the work reported in this paper.

Appendix A. Supplementary data

Supplementary material related to this article can be found online at https://doi.org/10.1016/j.catena.2026.109791.

References

Aguiar, Martín R., Sala, Osvaldo E., 1999. Patch structure, dynamics and implications for the functioning of arid ecosystems. Trends Ecol. Evolut. 14 (7), 273–277. http://dx.doi.org/10.1016/s0169-5347(99)01612-2.

Axelsson, Christoffer R., Hanan, Niall P., 2017. Patterns in woody vegetation structure across African Savannas. Biogeosciences 14 (13), 3239–3252. http://dx.doi.org/10.5194/bg-14-3239-2017.

Baartman, Jantiene E.M., Temme, Arnaud J.A.M., Saco, Patricia M., 2018. The effect of landform variation on vegetation patterning and related sediment dynamics. Earth Surf. Process. Landf. http://dx.doi.org/10.1002/esp.4377, arXiv:https://onlinelibrary.wiley.com/doi/pdf/10.1002/esp.4377. URL https://onlinelibrary.wiley.com/doi/abs/10.1002/esp.4377.

Bangen, Sara G., Wheaton, Joseph M., Bouwes, Nicolaas, Bouwes, Boyd, Jordan, Chris, 2014. A methodological intercomparison of topographic survey techniques for characterizing wadeable streams and rivers. Geomorphology 206, 343–361. http://dx.doi.org/10.1016/j.geomorph.2013.10.010.

Barbier, N., Couteron, P., Lejoly, J., Deblauwe, V., Lejeune, O., 2006. Self-organized vegetation patterning as a fingerprint of climate and human impact on semi-arid ecosystems. J. Ecol. (ISSN: 1365-2745) 94 (3), 537–547. http://dx.doi.org/10.1111/j.1365-2745.2006.01126.x.

Bastiaansen, Robbin, Jaïbi, Olfa, Deblauwe, Vincent, Eppinga, Maarten B., Siteur, Koen, Siero, Eric, Mermoz, Stéphane, Bouvet, Alexandre, Doelman, Arjen, Rietkerk, Max, 2018. Multistability of model and real dryland ecosystems through spatial self-organization. Proc. Natl. Acad. Sci. 115 (44), 11256–11261. http://dx.doi.org/10.1073/pnas.1804771115.

Bates, J.D., Svejcar, T., Miller, R.F., Angell, R.A., 2006. The effects of precipitation timing on sagebrush steppe vegetation. J. Arid. Environ. (ISSN: 0140-1963) 64 (4), 670–697. http://dx.doi.org/10.1016/j.jaridenv.2005.06.026, URL http://www.sciencedirect.com/science/article/pii/S0140196305001552.

Baudena, Mara, Rietkerk, Max, 2012. Complexity and coexistence in a simple spatial model for arid savanna ecosystems. Theor. Ecol. 6 (2), 131–141. http://dx.doi.org/10.1007/s12080-012-0165-1.

Bergkamp, G., Cerdà, A., Imeson, A.C., 1999. Magnitude-frequency analysis of water redistribution along a climate gradient in Spain. Catena 37 (1–2), 129–146. http://dx.doi.org/10.1016/s0341-8162(98)00058-7.

Bokulich, Alisa, 2014. How the tiger bush got its stripes: 'how possibly' vs. 'how actually'model explanations. Monist 97 (3), 321–338. http://dx.doi.org/10.5840/monist201497321.

Borgogno, F., D'Odorico, P., Laio, F., Ridolfi, L., 2009. Mathematical models of vegetation pattern formation in ecohydrology. Rev. Geophys. 47 (1), http://dx.doi.org/10.1029/2007RG000256.

Cammeraat, L.H, Imeson, A.C, 1999. The evolution and significance of soil–vegetation patterns following land abandonment and fire in Spain. Catena 37 (1–2), 107–127. http://dx.doi.org/10.1016/s0341-8162(98)00072-1.

Caviedes-Voullième, Daniel, Ahmadinia, Ebrahim, Hinz, Christoph, 2021. Interactions of microtopography, slope and infiltration cause complex rainfall-runoff behaviour at the hillslope scale for single rainfall events. Water Resour. Res. http://dx.doi.org/10.1029/2020wr028127.

Caviedes-Voullième, D., Fernández-Pato, J., Hinz, C., 2018. Cellular automata and finite volume solvers converge for 2D shallow flow modelling for hydrological modelling. J. Hydrol. 563, 411–417. http://dx.doi.org/10.1016/j.jhydrol.2018.06.021.

Caviedes-Voullième, Daniel, Fernández-Pato, Javier, Hinz, Christoph, 2020. Performance assessment of 2D zero-inertia and shallow water models for simulating rainfall-runoff processes. J. Hydrol. 124663. http://dx.doi.org/10.1016/j.jhydrol.2020.124663.

Caviedes-Voullième, Daniel, Hinz, Christoph, 2020. From non-equilibrium initial conditions to steady dryland vegetation patterns: how trajectories matter. Ecohydrology http://dx.doi.org/10.1002/eco.2199.

Caviedes-Voullième, Daniel, Morales-Hernández, Mario, Norman, Matthew R., Özgen-Xian, Ilhan, 2023. SERGHEI (SERGHEI-SWE) v1.0: a performance-portable high-performance parallel-computing shallow-water solver for hydrology and environmental hydraulics. Geosci. Model. Dev. 16 (3), 977–1008. http://dx.doi.org/10.5194/gmd-16-977-2023.

Caylor, Kelly K., Scanlon, Todd M., Rodriguez-Iturbe, Ignacio, 2009. Ecohydrological optimization of pattern and processes in water-limited ecosystems: A trade-off-based hypothesis. Water Resour. Res. 45 (8), n/a–n/a. http://dx.doi.org/10.1029/2008WR007230.

Cea, L., Garrido, M., Puertas, J., 2010. Experimental validation of two-dimensional depth-averaged models for forecasting rainfall–runoff from precipitation data in urban areas. J. Hydrol. 382 (1–4), 88–102. http://dx.doi.org/10.1016/j.jhydrol.2009.12.020.

Chamizo, Sonia, Cantón, Yolanda, Rodríguez-Caballero, Emilio, Domingo, Francisco, Escudero, Adrián, 2012. Runoff at contrasting scales in a semiarid ecosystem: A complex balance between biological soil crust features and rainfall characteristics. J. Hydrol. 452–453, 130–138. http://dx.doi.org/10.1016/j.jhydrol.2012.05.045.

Consolo, Giancarlo, Valenti, Giovanna, 2019. Secondary seed dispersal in the Klausmeier model of vegetation for sloped semi-arid environments. Ecol. Model. 402, 66–75. http://dx.doi.org/10.1016/j.ecolmodel.2019.02.009.

Costabile, P., Costanzo, C., Macchione, F., 2011. Comparative analysis of overland flow models using finite volume schemes. J. Hydroinform. (ISSN: 1464-7141) 14 (1), 122–135. http://dx.doi.org/10.2166/hydro.2011.077, arXiv:https://iwaponline.com/jh/article-pdf/14/1/122/386671/122.pdf.

Couteron, Pierre, 2002. Quantifying change in patterned semi-arid vegetation by Fourier analysis of digitized aerial photographs. Int. J. Remote Sens. 23 (17), 3407–3425. http://dx.doi.org/10.1080/01431160110107699.

Couteron, Pierre, Mahamane, Ali, Ouedraogo, Paul, Seghieri, Josiane, 2000. Differences between banded thickets (tiger bush) at two sites in West Africa. J. Veg. Sci. (ISSN: 1654-1103) 11 (3), 321–328. http://dx.doi.org/10.2307/3236624.

Cozzolino, Luca, Cimorelli, Luigi, Morte, Renata Della, Pugliano, Giovanni, Piscopo, Vincenzo, Pianese, Domenico, 2019. Flood propagation modelling with the local inertia approximation: theoretical and numerical analysis of its physical limitations. Adv. Water Resour. 103422. http://dx.doi.org/10.1016/j.advwatres.2019.103422.

Crompton, O., Katul, G., Lapides, D., Thompson, S., 2023. Hydrologic connectivity and patch-to-hillslope scale relations in dryland ecosystems. Geophys. Res. Lett. 50 (10), http://dx.doi.org/10.1029/2022gl101801.

Crompton, Octavia, Sytsma, Anneliese, Thompson, Sally, 2019. Emulation of the saint venant equations enables rapid and accurate predictions of infiltration and overland flow velocity on spatially heterogeneous surfaces. Water Resour. Res. 55 (8), 7108–7129. http://dx.doi.org/10.1029/2019wr025146.

Crompton, Octavia V., Thompson, Sally E., 2021. Sensitivity of dryland vegetation patterns to storm characteristics. Ecohydrology http://dx.doi.org/10.1002/eco.2269.

Cucchiaro, Sara, Cavalli, Marco, Vericat, Damià, Crema, Stefano, Llena, Manel, Beinat, Alberto, Marchi, Lorenzo, Cazorzi, Federico, 2019. Geomorphic effectiveness of check dams in a debris-flow catchment using multi-temporal topographic surveys. Catena 174, 73–83. http://dx.doi.org/10.1016/j.catena.2018.11.004.

Cueto-Felgueroso, Luis, Dentz, Marco, Juanes, Ruben, 2015. Regime shifts in bistable water-stressed ecosystems due to amplification of stochastic rainfall patterns. Phys. Rev. E 91 (5), http://dx.doi.org/10.1103/physreve.91.052148.

Dagbovie, A.S., Sherratt, J.A., 2014. Pattern selection and hysteresis in the rietkerk model for banded vegetation in semi-arid environments. J. R. Soc. Interface 11 (99), http://dx.doi.org/10.1098/rsif.2014.0465, 20140465–20140465.

de Almeida, Gustavo A.M., Bates, Paul, 2013. Applicability of the local inertial approximation of the shallow water equations to flood modeling. Water Resour. Res. 49 (8), 4833–4844. http://dx.doi.org/10.1002/wrcr.20366.

DeAngelis, Donald L., 2012. Self-organizing processes in landscape pattern and resilience: A review. ISRN Ecol. 2012, 1–18. http://dx.doi.org/10.5402/2012/274510.

Deblauwe, Vincent, Barbier, Nicolas, Couteron, Pierre, Lejeune, Olivier, Bogaert, Jan, 2008. The global biogeography of semi-arid periodic vegetation patterns. Glob. Ecol. Biogeogr. (ISSN: 1466-8238) 17 (6), 715–723. http://dx.doi.org/10.1111/j.1466-8238.2008.00413.x.

Deblauwe, Vincent, Couteron, Pierre, Bogaert, Jan, Barbier, Nicolas, 2012. Determinants and dynamics of banded vegetation pattern migration in arid climates. Ecol. Monograph. 82 (1), 3–21. http://dx.doi.org/10.1890/11-0362.1.

Deblauwe, Vincent, Couteron, Pierre, Lejeune, Olivier, Bogaert, Jan, Barbier, Nicolas, 2011. Environmental modulation of self-organized periodic vegetation patterns in Sudan. Ecography (ISSN: 1600-0587) 34 (6), 990–1001. http://dx.doi.org/10.1111/j.1600-0587.2010.06694.x.

Djebou, Dagbegnon C. Sohoulande, Singh, Vijay P., Frauenfeld, Oliver W., 2015. Vegetation response to precipitation across the aridity gradient of the southwestern united states. J. Arid. Environ. (ISSN: 0140-1963) 115, 35–43. http://dx.doi.org/10.1016/j.jaridenv.2015.01.005, URL http://www.sciencedirect.com/science/article/pii/S0140196315000063.

Dottori, F., Todini, E., 2011. Developments of a flood inundation model based on the cellular automata approach: Testing different methods to improve model performance. Phys. Chem. Earth Parts A/B/C (ISSN: 1474-7065) 36 (7–8), 266–280. http://dx.doi.org/10.1016/j.pce.2011.02.004, URL http://www.sciencedirect.com/science/article/pii/S1474706511000362. Recent Advances in Mapping and Modelling Flood Processes in Lowland Areas.

Dunkerley, D.L., 1997. Banded vegetation: development under uniform rainfall from a simple cellular automaton model. Plant Ecol. (ISSN: 1573-5052) 129 (2), 103–111. http://dx.doi.org/10.1023/A:1009725732740.

Dunkerley, D., 2002a. Infiltration rates and soil moisture in a groved mulga community near Alice Springs, arid central Australia: evidence for complex internal rainwater redistribution in a runoff–runon landscape. J. Arid. Environ. 51 (2), 199–219. http://dx.doi.org/10.1006/jare.2001.0941.

Dunkerley, David, 2002b. Systematic variation of soil infiltration rates within and between the components of the vegetation mosaic in an Australian desert landscape. Hydrol. Process. 16 (1), 119–131. http://dx.doi.org/10.1002/hyp.357.

Dunkerley, D., 2018a. Banded vegetation in some Australian semi-arid landscapes: 20 years of field observations to support the development and evaluation of numerical models of vegetation pattern evolution. Desert (ISSN: 2008-0875) 23 (2), 165–187.

Dunkerley, David, 2018b. How does sub-hourly rainfall intermittency bias the climatology of hourly and daily rainfalls? Examples from arid and wet tropical Australia. Int. J. Climatol. http://dx.doi.org/10.1002/joc.5961.

Dunkerley, David, 2018c. How is overland flow produced under intermittent rain? An analysis using plot-scale rainfall simulation on dryland soils. J. Hydrol. (ISSN: 0022-1694) 556, 119–130. http://dx.doi.org/10.1016/j.jhydrol.2017.11.003, URL http://www.sciencedirect.com/science/article/pii/S0022169417307576.

Dunkerley, D.L, Brown, K.J, 1999. Banded vegetation near Broken Hill, Australia: significance of surface roughness and soil physical properties. Catena 37 (1–2), 75–88. http://dx.doi.org/10.1016/s0341-8162(98)00056-3.

Eddy, J., Humphreys, G.S., Hart, D.M., Mitchell, P.B., Fanning, P.C., 1999. Vegetation arcs and litter dams: similarities and differences. Catena (ISSN: 0341-8162) 37 (1), 57–73. http://dx.doi.org/10.1016/S0341-8162(98)00055-1, URL http://www.sciencedirect.com/science/article/pii/S0341816298000551.

Eigentler, Lukas, Sherratt, Jonathan A., 2018. Analysis of a model for banded vegetation patterns in semi-arid environments with nonlocal dispersal. J. Math. Biol. 77 (3), 739–763. http://dx.doi.org/10.1007/s00285-018-1233-y.

Eigentler, L., Sherratt, J.A., 2022. Long-range seed dispersal enables almost stationary patterns in a model for dryland vegetation. J. Math. Biol. 86 (1), http://dx.doi.org/10.1007/s00285-022-01852-x.

Esteban, Julien, Fairén, Victor, 2006. Self-organized formation of banded vegetation patterns in semi-arid regions: A model. Ecol. Complex. (ISSN: 1476-945X) 3 (2), 109–118. http://dx.doi.org/10.1016/j.ecocom.2005.10.001, URL http://www.sciencedirect.com/science/article/pii/S1476945X05000851.

Estes, Lyndon, Elsen, Paul R., Treuer, Timothy, Ahmed, Labeeb, Caylor, Kelly, Chang, Jason, Choi, Jonathan J., Ellis, Erle C., 2018. The spatial and temporal domains of modern ecology. Nat. Ecol. Evol. 2 (5), 819–826. http://dx.doi.org/10.1038/s41559-018-0524-4.

Farguell, Joaquim, Úbeda, Xavier, Pacheco, Edinson, 2022. Shrub removal effects on runoff and sediment transport in a mediterranean experimental catchment (Vernegà River, NE Spain). Catena 210, 105882. http://dx.doi.org/10.1016/j.catena.2021.105882.

Fatichi, Simone, Vivoni, Enrique R., Ogden, Fred L., Ivanov, Valeriy Y., Mirus, Benjamin, Gochis, David, Downer, Charles W., Camporese, Matteo, Davison, Jason H., Ebel, Brian, Jones, Norm, Kim, Jongho, Mascaro, Giuseppe, Niswonger, Richard, Restrepo, Pedro, Rigon, Riccardo, Shen, Chaopeng, Sulis, Mauro, Tarboton, David, 2016. An overview of current applications, challenges, and future trends in distributed process-based models in hydrology. J. Hydrol. (ISSN: 0022-1694) 537, 45–60. http://dx.doi.org/10.1016/j.jhydrol.2016.03.026, URL http://www.sciencedirect.com/science/article/pii/S0022169416301317.

Fernández, R.J., 2007. On the frequent lack of response of plants to rainfall events in arid areas. J. Arid. Environ. (ISSN: 0140-1963) 68 (4), 688–691. http://dx.doi.org/10.1016/j.jaridenv.2006.07.004, URL http://www.sciencedirect.com/science/article/pii/S0140196306002291.

Fernández-Pato, J., Caviedes-Voullième, D., García-Navarro, P., 2016. Rainfall/runoff simulation with 2D full shallow water equations: sensitivity analysis and calibration of infiltration parameters. J. Hydrol. 536, 496–513. http://dx.doi.org/10.1016/j.jhydrol.2016.03.021.

Fiorillo, Edoardo, Maselli, Fabio, Tarchiani, Vieri, Vignaroli, Patrizio, 2017. Analysis of land degradation processes on a tiger bush plateau in South West Niger using MODIS and LANDSAT TM/ETM+ data. Int. J. Appl. Earth Obs. Geoinf. 62, 56–68. http://dx.doi.org/10.1016/j.jag.2017.05.010.

Foti, R., Ramírez, J.A., 2013. A mechanistic description of the formation and evolution of vegetation patterns. Hydrol. Earth Syst. Sci. 17 (1), 63–84. http://dx.doi.org/10.5194/hess-17-63-2013.

Galle, S., Ehrmann, M., Peugeot, C., 1999. Water balance in a banded vegetation pattern. Catena 37 (1–2), 197–216. http://dx.doi.org/10.1016/s0341-8162(98)90060-1.

Gandhi, Punit, Werner, Lucien, Iams, Sarah, Gowda, Karna, Silber, Mary, 2018. A topographic mechanism for arcing of dryland vegetation bands. J. R. Soc. Interface 15 (147), 20180508. http://dx.doi.org/10.1098/rsif.2018.0508.

Gilad, E., von Hardenberg, J., Provenzale, A., Shachak, M., Meron, E., 2007. A mathematical model of plants as ecosystem engineers. J. Theoret. Biol. (ISSN: 0022-5193) 244 (4), 680–691. http://dx.doi.org/10.1016/j.jtbi.2006.08.006, URL http://www.sciencedirect.com/science/article/pii/S0022519306003493.

Gowda, Karna, Iams, Sarah, Silber, Mary, 2018. Signatures of human impact on self-organized vegetation in the horn of Africa. Sci. Rep. (ISSN: 2045-2322) 8 (1), 3622.

Groner, Elli, Babad, Avshalom, Swiderski, Naomi Berda, Shachak, Moshe, 2023. Toward an extreme world: The hyper-arid ecosystem as a natural model. Ecosphere 14 (6), http://dx.doi.org/10.1002/ecs2.4586.

Grünzweig, José M., Boeck, Hans J. De, Rey, Ana, Santos, Maria J., Adam, Ori, Bahn, Michael, Belnap, Jayne, Deckmyn, Gaby, Dekker, Stefan C., Flores, Omar, Gliksman, Daniel, Helman, David, Hultine, Kevin R., Liu, Lingli, Meron, Ehud, Michael, Yaron, Sheffer, Efrat, Throop, Heather L., Tzuk, Omer, Yakir, Dan, 2022. Dryland mechanisms could widely control ecosystem functioning in a drier and warmer world. Nat. Ecol. Evol. http://dx.doi.org/10.1038/s41559-022-01779-y.

Gutiérrez-Jurado, Hugo A., Vivoni, Enrique R., Cikoski, Colin, Harrison, J. Bruce J., Bras, Rafael L., Istanbulluoglu, Erkan, 2013. On the observed ecohydrologic dynamics of a semiarid basin with aspect-delimited ecosystems. Water Resour. Res. (ISSN: 1944-7973) 49 (12), 8263–8284. http://dx.doi.org/10.1002/2013WR014364.

Guttal, Vishwesha, Jayaprakash, C., 2007. Self-organization and productivity in semi-arid ecosystems: Implications of seasonality in rainfall. J. Theoret. Biol. 248 (3), 490–500. http://dx.doi.org/10.1016/j.jtbi.2007.05.020.

Hemming, C.F., 1965. Vegetation arcs in Somaliland. J. Ecol. 53 (1), 57. http://dx.doi.org/10.2307/2257565.

Moreno de las Heras, Mariano, Merino-Martín, Luis, Saco, Patricia M., Espigares, Tíscar, Gallart, Francesc, Nicolau, José M., 2020. Structural and functional control of surface-patch to hillslope runoff and sediment connectivity in Mediterranean dry reclaimed slope systems. Hydrol. Earth Syst. Sci. 24 (5), 2855–2872. http://dx.doi.org/10.5194/hess-24-2855-2020.

Moreno de las Heras, Mariano, Saco, Patricia M., Willgoose, Garry R., Tongway, David J., 2011. Assessing landscape structure and pattern fragmentation in semiarid ecosystems using patch-size distributions. Ecol. Appl. 21 (7), 2793–2805. http://dx.doi.org/10.1890/10-2113.1.

Moreno de las Heras, Mariano, Saco, Patricia M., Willgoose, Garry R., Tongway, David J., 2012. Variations in hydrological connectivity of Australian semiarid landscapes indicate abrupt changes in rainfall-use efficiency of vegetation. J. Geophys. Res.: Biogeosci. 117 (G3), n/a–n/a. http://dx.doi.org/10.1029/2011jg001839.

HilleRisLambers, Reinier, Rietkerk, Max, van den Bosch, Frank, Prins, Herbert H.T., de Kroon, Hans, 2001. Vegetation pattern formation in semi-arid grazing systems. Ecology 82 (1), 50–61. http://dx.doi.org/10.1890/0012-9658(2001)082[0050:VPFISA]2.0.CO;2.

Kästner, Karl, Caviedes-Voullième, Daniel, Hinz, Christoph, 2025. Formation of spatial vegetation patterns in heterogeneous environments. PLoS One (ISSN: 1932-6203) 20 (5), e0324181. http://dx.doi.org/10.1371/journal.pone.0324181.

Kästner, Karl, van de Vijsel, Roeland C., Caviedes-Voullième, Daniel, Frechen, Nanu T., Hinz, Christoph, 2024. Unravelling the spatial structure of regular dryland vegetation patterns. Catena (ISSN: 0341-8162) 247, 108442. http://dx.doi.org/10.1016/j.catena.2024.108442.

Kéfi, Sonia, Couteron, Pierre, 2018. Spatiotemporal patterns as indicators of approaching critical transitions. Ecol. Indic. 94, 491–493. http://dx.doi.org/10.1016/j.ecolind.2018.07.034.

Khosh Bin Ghomash, S., Apel, H., Caviedes-Voullième, D., 2024. Are 2D shallow-water solvers fast enough for early flood warning? A comparative assessment on the 2021 ahr valley flood event. Nat. Hazards Earth Syst. Sci. 24 (8), 2857–2874. http://dx.doi.org/10.5194/nhess-24-2857-2024, URL https://nhess.copernicus.org/articles/24/2857/2024/.

Khosh Bin Ghomash, S., Caviedes-Voullième, Daniel, Hinz, Christoph, 2019. Effects of erosion-induced changes to topography on runoff dynamics. J. Hydrol. 573, 811–828. http://dx.doi.org/10.1016/j.jhydrol.2019.04.018.

Klausmeier, C.A., 1999. Regular and irregular patterns in semiarid vegetation. Science 284 (5421), 1826–1828. http://dx.doi.org/10.1126/science.284.5421.1826.

Kletter, A.Y., von Hardenberg, J., Meron, E., Provenzale, A., 2009. Patterned vegetation and rainfall intermittency. J. Theoret. Biol. (ISSN: 0022-5193) 256 (4), 574–583. http://dx.doi.org/10.1016/j.jtbi.2008.10.020, URL http://www.sciencedirect.com/science/article/pii/S0022519308005614.

Köhnke, M., Malchow, H., 2017. Impact of parameter variability and environmental noise on the Klausmeier model of vegetation pattern formation. Mathematics 5 (4), 69. http://dx.doi.org/10.3390/math5040069.

Lázaro, R., Rodrigo, F.S., Gutiérrez, L., Domingo, F., Puigdefábregas, J., 2001. Analysis of a 30-year rainfall record (1967–1997) in semi–arid SE Spain for implications on vegetation. J. Arid. Environ. 48 (3), 373–395. http://dx.doi.org/10.1006/jare.2000.0755.

Le, Phong V.V., Kumar, Praveen, 2017. Interaction between ecohydrologic dynamics and microtopographic variability under climate change. Water Resour. Res. (ISSN: 1944-7973) 53 (10), 8383–8403. http://dx.doi.org/10.1002/2017WR020377.

Lefever, R., Lejeune, O., 1997. On the origin of tiger bush. Bull. Math. Biol. (ISSN: 0092-8240) 59 (2), 263–294. http://dx.doi.org/10.1016/S0092-8240(96)00072-9, URL http://www.sciencedirect.com/science/article/pii/S0092824096000729.

Lejeune, Olivier, Tlidi, Mustapha, Lefever, René, 2004. Vegetation spots and stripes: Dissipative structures in arid landscapes. Int. J. Quantum Chem. (ISSN: 1097-461X) 98 (2), 261–271. http://dx.doi.org/10.1002/qua.10878.

Leprun, Jean Claude, 1999. The influences of ecological factors on tiger bush and dotted bush patterns along a gradient from mali to northern Burkina Faso. Catena 37 (1–2), 25–44. http://dx.doi.org/10.1016/s0341-8162(98)00054-x.

Ludwig, John A., Bastin, Gary N., Chewings, Vanessa H., Eager, Robert W., Liedloff, Adam C., 2007. Leakiness: A new index for monitoring the health of arid and semiarid landscapes using remotely sensed vegetation cover and elevation data. Ecol. Indic. 7 (2), 442–454. http://dx.doi.org/10.1016/j.ecolind.2006.05.001.

Ludwig, John A., Wilcox, Bradford P., Breshears, David D., Tongway, David J., Imeson, Anton C., 2005. Vegetation patches and runoff-erosion as interacting ecohydrological processesi n semiarid landscapes. Ecology (ISSN: 1939-9170) 86 (2), 288–297. http://dx.doi.org/10.1890/03-0569.

Mabbutt, J.A., Fanning, P.C., 1987. Vegetation banding in arid Western-Australia. J. Arid. Environ. (ISSN: 0140-1963) 12 (1), 41–59.

Macfadyen, W.A., 1950. Vegetation patterns in the semi-desert plains of British Somaliland. Geogr. J. 116 (4/6), 199. http://dx.doi.org/10.2307/1789384.

Mander, Luke, Dekker, Stefan C., Li, Mao, Mio, Washington, Punyasena, Surangi W., Lenton, Timothy M., 2017. A morphometric analysis of vegetation patterns in dry-land ecosystems. R. Soc. Open Sci. 4 (2), http://dx.doi.org/10.1098/rsos.160443, URL http://rsos.royalsocietypublishing.org/content/4/2/160443.

Mayor, Ángeles G., Bautista, Susana, Small, Eric E., Dixon, Mike, Bellot, Juan, 2008. Measurement of the connectivity of runoff source areas as determined by vegetation pattern and topography: A tool for assessing potential water and soil losses in drylands. Water Resour. Res. 44 (10), n/a–n/a. http://dx.doi.org/10.1029/2007WR006367.

McDonald, Alyson K., Kinucan, Robert J., Loomis, Lynn E., 2009. Ecohydrological interactions within banded vegetation in the northeastern Chihuahuan Desert, USA. Ecohydrology 2 (1), 66–71. http://dx.doi.org/10.1002/eco.40.

McGrath, Gavan S., Paik, Kyungrock, Hinz, Christoph, 2012. Microtopography alters self-organized vegetation patterns in water-limited ecosystems. J. Geophys. Res.: Biogeosci. 117 (G3), n/a–n/a. http://dx.doi.org/10.1029/2011JG001870.

Meron, Ehud, 2016. Pattern formation – a missing link in the study of ecosystem response to environmental changes. Math. Biosci. 271, 1–18. http://dx.doi.org/10.1016/j.mbs.2015.10.015.

Meron, Ehud, 2018. From patterns to function in living systems: Dryland ecosystems as a case study. Annu. Rev. Condens. Matter Phys. 9 (1), 79–103. http://dx.doi.org/10.1146/annurev-conmatphys-033117-053959.

Meron, Ehud, Gilad, Erez, von Hardenberg, Jost, Shachak, Moshe, Zarmi, Yair, 2004. Vegetation patterns along a rainfall gradient. Chaos Solitons Fractals 19 (2), 367–376. http://dx.doi.org/10.1016/S0960-0779(03)00049-3.

Modarres, Reza, de Paulo Rodrigues da Silva, Paulo, 2007. Rainfall trends in arid and semi-arid regions of Iran. J. Arid. Environ. (ISSN: 0140-1963) 70 (2), 344–355. http://dx.doi.org/10.1016/j.jaridenv.2006.12.024, URL http://www.sciencedirect.com/science/article/pii/S0140196307000225.

Montaña, C., 1992. The colonization of bare areas in 2-phase mosaics of an arid ecosystem. J. Ecol.

Montana, C., Seghieri, Josiane, Cornet, Antoine, 2001. Vegetation dynamics : recruitment and regeneration in two-phase mosaics. In: Banded Vegetation Patterning in Arid and Semiarid Environments : Ecological Processes and Consequences for Management. In: Ecological Studies, Springer, (ISSN: 0070-8356) pp. 132–145, URL http://www.documentation.ird.fr/hor/fdi:010025910.

Moudrý, Vítězslav, Lecours, Vincent, Gdulová, Kateřina, Gábor, Lukáš, Moudrá, Lucie, Kropáček, Jan, Wild, Jan, 2018. On the use of global DEMs in ecological modelling and the accuracy of new bare-earth DEMs. Ecol. Model. 383, 3–9. http://dx.doi.org/10.1016/j.ecolmodel.2018.05.006.

Mounirou, Lawani Adjadi, Yonaba, Roland, Koïta, Mahamadou, Paturel, Jean-Emmanuel, Mahé, Gil, Yacouba, Hamma, Karambiri, Harouna, 2021. Hydrologic similarity: Dimensionless runoff indices across scales in a semi-arid catchment. J. Arid. Environ. 193, 104590. http://dx.doi.org/10.1016/j.jaridenv.2021.104590.

Ogle, Kiona, Barber, Jarrett J., Barron-Gafford, Greg A., Bentley, Lisa Patrick, Young, Jessica M., Huxman, Travis E., Loik, Michael E., Tissue, David T., 2015. Quantifying ecological memory in plant and ecosystem processes. Ecol. Lett. (ISSN: 1461-0248) 18 (3), 221–235. http://dx.doi.org/10.1111/ele.12399.

Okin, Gregory S., de las Heras, Mariano Moreno, Saco, Patricia M., Throop, Heather L., Vivoni, Enrique R., Parsons, Anthony J., Wainwright, John, Peters, Debra P.C., 2015. Connectivity in dryland landscapes: shifting concepts of spatial interactions. Front. Ecol. Environ. 13 (1), 20–27. http://dx.doi.org/10.1890/140163.

Panthou, G., Lebel, T., Vischel, T., Quantin, G., Sane, Y., Ba, A., Ndiaye, O., Diongue-Niang, A., Diopkane, M., 2018. Rainfall intensification in tropical semi-arid regions: the Sahelian case. Environ. Res. Lett. 13 (6), 064013. http://dx.doi.org/10.1088/1748-9326/aac334.

Pappas, Christoforos, Fatichi, Simone, Rimkus, Stefan, Burlando, Paolo, Huber, Markus O., 2015. The role of local-scale heterogeneities in terrestrial ecosystem modeling. J. Geophys. Res.: Biogeosci. (ISSN: 2169-8961) 120 (2), 341–360. http://dx.doi.org/10.1002/2014JG002735, 2014JG002735.

Paschalis, Athanasios, Katul, Gabriel G., Fatichi, Simone, Manoli, Gabriele, Molnar, Peter, 2016. Matching ecohydrological processes and scales of banded vegetation patterns in semiarid catchments. Water Resour. Res. 52 (3), 2259–2278. http://dx.doi.org/10.1002/2015WR017679.

Pelletier, Jon D., DeLong, Stephen B., Orem, Caitlin A., Becerra, Patricio, Compton, Kathleen, Gressett, Katrina, Lyons-Baral, John, McGuire, Luke A., Molaro, Jamie L., Spinler, Joshua C., 2012. How do vegetation bands form in dry lands? Insights from numerical modeling and field studies in southern Nevada, USA. J. Geophys. Res.: Earth Surf. (ISSN: 2156-2202) 117 (F4), n/a–n/a. http://dx.doi.org/10.1029/2012JF002465.

Penny, G.G., Daniels, K.E., Thompson, S.E., 2013. Local properties of patterned vegetation: quantifying endogenous and exogenous effects. Philos. Trans. R. Soc. A: Math. Phys. Eng. Sci. 371 (2004), http://dx.doi.org/10.1098/rsta.2012.0359, 20120359–20120359.

Pinto-Ramos, D., Clerc, M.G., Tlidi, M., 2023. Topological defects law for migrating banded vegetation patterns in arid climates. Sci. Adv. 9 (31), http://dx.doi.org/10.1126/sciadv.adf6620.

Pueyo, Y., Kefi, S., Alados, C.L., Rietkerk, M., 2008. Dispersal strategies and spatial organization of vegetation in arid ecosystems. Oikos (ISSN: 0030-1299) 117 (10), 1522–1532. http://dx.doi.org/10.1111/j.2008.0030-1299.16735.x.

Pueyo, Y., Kefi, S., Diaz-Sierra, R., Alados, C.L., Rietkerk, M., 2010. The role of reproductive plant traits and biotic interactions in the dynamics of semi-arid plant communities. Theor. Popul. Biol. (ISSN: 0040-5809) 78 (4), 289–297. http://dx.doi.org/10.1016/j.tpb.2010.09.001.

Puigdefábregas, Juan, 2005. The role of vegetation patterns in structuring runoff and sediment fluxes in drylands. Earth Surf. Process. Landf. 30 (2), 133–147. http://dx.doi.org/10.1002/esp.1181.

Rietkerk, M., Boerlijst, M.C., van Langevelde, F., HilleRisLambers, R., van de Koppel, J., Kumar, L., Prins, H.H.T., de Roos, A.M., 2002. Self-organization of vegetation in arid ecosystems. Amer. Nat. (ISSN: 0003-0147) 160 (4), 524–530. http://dx.doi.org/10.1086/342078.

Rodríguez-Caballero, E., Lázaro, R., Cantón, Y., Puigdefabregas, J., Solé-Benet, A., 2018. Long-term hydrological monitoring in arid-semiarid Almería, SE Spain. what have we learned? Cuad. Investig. Geogr. (ISSN: 1697-9540) http://dx.doi.org/10.18172/cig.3462, URL https://publicaciones.unirioja.es/ojs/index.php/cig/article/view/3462.

Roitberg, Elena, Shoshany, Maxim, 2017. Can spatial patterns along climatic gradients predict ecosystem responses to climate change? Experimenting with reaction-diffusion simulations. PLoS One 12 (4), 1–12. http://dx.doi.org/10.1371/journal.pone.0174942.

Saco, Patricia M., Moreno de las Heras, Mariano, 2013. Ecogeomorphic coevolution of semiarid hillslopes: Emergence of banded and striped vegetation patterns through interaction of biotic and abiotic processes. Water Resour. Res. 49 (1), 115–126. http://dx.doi.org/10.1029/2012WR012001.

Saco, Patricia M., de las Heras, Mariano Moreno, Keesstra, Saskia, Baartman, Jantiene, Yetemen, Omer, Rodríguez, José F., 2018. Vegetation and soil degradation in drylands: Non linear feedbacks and early warning signals. Curr. Opin. Environ. Sci. Health 5, 67–72. http://dx.doi.org/10.1016/j.coesh.2018.06.001.

Saco, Patricia M., Rodríguez, José F., de las Heras, Mariano Moreno, Keesstra, Saskia, Azadi, Samira, Sandi, Steven, Baartman, Jantiene, Rodrigo-Comino, Jesús, Rossi, María Julieta, 2020. Using hydrological connectivity to detect transitions and degradation thresholds: Applications to dryland systems. Catena 186, 104354. http://dx.doi.org/10.1016/j.catena.2019.104354.

Saco, P.M., Willgoose, G.R., Hancock, G.R., 2007. Eco-geomorphology of banded vegetation patterns in arid and semi-arid regions. Hydrol. Earth Syst. Sci. 11 (6), 1717–1730. http://dx.doi.org/10.5194/hess-11-1717-2007, URL https://www.hydrol-earth-syst-sci.net/11/1717/2007/.

Santillana, Mauricio, Dawson, Clint, 2010. A numerical approach to study the properties of solutions of the diffusive wave approximation of the shallow water equations. Comput. Geosci. (ISSN: 1420-0597) 14 (1), 31–53. http://dx.doi.org/10.1007/s10596-009-9131-4.

Schwinning, Susan, Sala, Osvaldo E., Loik, Michael E., Ehleringer, James R., 2004. Thresholds, memory, and seasonality: understanding pulse dynamics in arid/semi-arid ecosystems. Oecologia (ISSN: 1432-1939) 141 (2), 191–193. http://dx.doi.org/10.1007/s00442-004-1683-3.

Sherratt, J.A., 2011. Pattern solutions of the klausmeier model for banded vegetation in semi-arid environments II: patterns with the largest possible propagation speeds. Proc. R. Soc. A: Math. Phys. Eng. Sci. 467 (2135), 3272–3294. http://dx.doi.org/10.1098/rspa.2011.0194.

Sherratt, Jonathan A., 2013. History-dependent patterns of whole ecosystems. Ecol. Complex. (ISSN: 1476-945X) 14, 8–20. http://dx.doi.org/10.1016/j.ecocom.2012.12.002, URL http://www.sciencedirect.com/science/article/pii/S1476945X13000020. Special Issue on the occasion of Horst Malchow's 60th birthday.

Sherratt, Jonathan A., 2015. Using wavelength and slope to infer the historical origin of semiarid vegetation bands. Proc. Natl. Acad. Sci. 112 (14), 4202–4207. http://dx.doi.org/10.1073/pnas.1420171112, URL http://www.pnas.org/content/112/14/4202.abstract.

Sherratt, Jonathan A., 2016. When does colonisation of a semi-arid hillslope generate vegetation patterns? J. Math. Biol. 73 (1), 199–226. http://dx.doi.org/10.1007/s00285-015-0942-8.

Siteur, Koen, Eppinga, Maarten B., Karssenberg, Derek, Baudena, Mara, Bierkens, Marc F.P., Rietkerk, Max, 2014a. How will increases in rainfall intensity affect semiarid ecosystems? Water Resour. Res. 50 (7), 5980–6001. http://dx.doi.org/10.1002/2013WR014955.

Siteur, Koen, Siero, Eric, Eppinga, Maarten B., Rademacher, Jens, Doelman, Arjen, Rietkerk, Max, 2014b. Beyond turing: The response of patterned ecosystems to environmental change. Ecol. Complex. 20, 81–96. http://dx.doi.org/10.1016/j.ecocom.2014.09.002.

Stewart, J., Parsons, A.J., Wainwright, J., Okin, G.S., Bestelmeyer, B.T., Fredrickson, E.L., Schlesinger, W.H., 2014. Modeling emergent patterns of dynamic desert ecosystems. Ecol. Monograph. 84 (3), 373–410. http://dx.doi.org/10.1890/12-1253.1.

Sun, Gui-Quan, Jin, Zhen, Tan, Qiulin, 2010. Measurement of self-organization in arid ecosystems. J. Biol. Systems (ISSN: 0218-3390) 18 (2), 495–508. http://dx.doi.org/10.1142/S0218339010003366.

Sun, Gui-Quan, Li, Jing, Yu, Benguo, Jin, Zhen, 2013. Noise induced pattern transition in a vegetation model. Appl. Math. Comput. (ISSN: 0096-3003) 221, 463–468. http://dx.doi.org/10.1016/j.amc.2013.06.072, URL http://www.sciencedirect.com/science/article/pii/S0096300313007212.

Svoray, Tal, Sela, Shai, Chen, Li, Assouline, Shmuel, 2021. Lateral flow and contributing area control vegetation cover in a semiarid environment. Water Resour. Res. http://dx.doi.org/10.1029/2021wr030998.

Thiery, J.M., D'Herbes, J.-M., Valentin, C., 1995. A model simulating the genesis of banded vegetation patterns in Niger. J. Ecol. 83 (3), 497–507, URL http://www.jstor.org/stable/2261603 (ISSN: 00220477, 13652745).

Thompson, Sally E., Assouline, Shmuel, Chen, Li, Trahktenbrot, Ana, Svoray, Tal, Katul, Gabriel G., 2014. Secondary dispersal driven by overland flow in drylands: Review and mechanistic model development. Mov. Ecol. (ISSN: 2051-3933) 2 (1), 7. http://dx.doi.org/10.1186/2051-3933-2-7.

Thompson, Sally, Katul, Gabriel, 2009. Secondary seed dispersal and its role in landscape organization. Geophys. Res. Lett. (ISSN: 1944-8007) 36 (2), n/a–n/a. http://dx.doi.org/10.1029/2008GL036044, L02402.

Thompson, Sally, Katul, Gabriel, Konings, Alexandra, Ridolfi, Luca, 2011. Unsteady overland flow on flat surfaces induced by spatial permeability contrasts. Adv. Water Resour. 34 (8), 1049–1058. http://dx.doi.org/10.1016/j.advwatres.2011.05.012.

Tongway, David J., Valentin, Christian, Seghieri, Josiane, 2001. Banded vegetation patterning in arid and semiarid environments: Ecological processes and consequences for management, first ed. In: Ecological Studies 149, Springer-Verlag New York, URL http://gen.lib.rus.ec/book/index.php?md5=8D736B97B87287338C3F2F28988B11AF ISBN: 978-1-4612-6559-7, 978-1-4613-0207-0.

Trichon, Valérie, Hiernaux, Pierre, Walcker, Romain, Mougin, Eric, 2018. The persistent decline of patterned woody vegetation: The tiger bush in the context of the regional Sahel greening trend. Global Change Biol. 24 (6), 2633–2648. http://dx.doi.org/10.1111/gcb.14059.

Tsai, Christina W., 2003. Applicability of kinematic, noninertia, and quasi-steady dynamic wave models to unsteady flow routing. J. Hydraul. Eng. 129 (8), 613–627. http://dx.doi.org/10.1061/(asce)0733-9429(2003)129:8(613).

Ursino, Nadia, 2005. The influence of soil properties on the formation of unstable vegetation patterns on hillsides of semiarid catchments. Adv. Water Resour. 28 (9), 956–963. http://dx.doi.org/10.1016/j.advwatres.2005.02.009.

Ursino, N., 2007. Modeling banded vegetation patterns in semiarid regions: Interdependence between biomass growth rate and relevant hydrological processes. Water Resour. Res. (ISSN: 1944-7973) 43 (4), n/a–n/a. http://dx.doi.org/10.1029/2006WR005292, W04412.

Ursino, Nadia, Contarini, Samuel, 2006. Stability of banded vegetation patterns under seasonal rainfall and limited soil moisture storage capacity. Adv. Water Resour. 29 (10), 1556–1564. http://dx.doi.org/10.1016/j.advwatres.2005.11.006.

Valentin, C., d'Herbès, J.M, 1999. Niger tiger bush as a natural water harvesting system. Catena 37 (1–2), 231–256. http://dx.doi.org/10.1016/s0341-8162(98)00061-7.

Valentin, C., d'Herbès, J.M, Poesen, J., 1999. Soil and water components of banded vegetation patterns. Catena (ISSN: 0341-8162) 37 (1?2), 1–24. http://dx.doi.org/10.1016/S0341-8162(99)00053-3, URL http://www.sciencedirect.com/science/article/pii/S0341816299000533.

Vega, E., Montaña, C., 2011. Effects of overgrazing and rainfall variability on the dynamics of semiarid banded vegetation patterns: A simulation study with cellular automata. J. Arid. Environ. 75 (1), 70–77. http://dx.doi.org/10.1016/j.jaridenv.2010.08.001.

Vericat, D., Smith, M.W., Brasington, J., 2014. Patterns of topographic change in sub-humid badlands determined by high resolution multi-temporal topographic surveys. Catena 120, 164–176. http://dx.doi.org/10.1016/j.catena.2014.04.012.

Vico, Giulia, Thompson, Sally E., Manzoni, Stefano, Molini, Annalisa, Albertson, John D., Almeida-Cortez, Jarcilene S., Fay, Philip A., Feng, Xue, Guswa, Andrew J., Liu, Hu, Wilson, Tiffany G., Porporato, Amilcare, 2014. Climatic, ecophysiological, and phenological controls on plant ecohydrological strategies in seasonally dry ecosystems. Ecohydrology 8 (4), 660–681. http://dx.doi.org/10.1002/eco.1533.

von Hardenberg, J., Meron, E., Shachak, M., Zarmi, Y., 2001. Diversity of vegetation patterns and desertification. Phys. Rev. Lett. 87 (19), http://dx.doi.org/10.1103/PhysRevLett.87.198101.

Wang, Yueling, Liang, Qiuhua, Kesserwani, Georges, Hall, Jim W., 2011. A positivity-preserving zero-inertia model for flood simulation. Comput. & Fluids (ISSN: 0045-7930) 46 (1, SI), 505–511. http://dx.doi.org/10.1016/j.compfluid.2011.01.026, 10th Institute for Computational Fluid Dynamics (ICFD) Conference, Univ Reading, ENGLAND, 2010.

Wu, X.B., Thurow, T.L., Whisenant, S.G., 2000. Fragmentation and changes in hydrologic function of tiger bush landscapes, south-west Niger. J. Ecol. 88 (5), 790–800, URL http://www.jstor.org/stable/2648339 (ISSN: 00220477, 13652745).

Yizhaq, Hezi, Gilad, Erez, Meron, Ehud, 2005. Banded vegetation: biological productivity and resilience. Phys. A 356 (1), 139–144. http://dx.doi.org/10.1016/j.physa.2005.05.026.

Zelnik, Yuval R., Kinast, Shai, Yizhaq, Hezi, Bel, Golan, Meron, Ehud, 2013. Regime shifts in models of dryland vegetation. Philos. Trans. R. Soc. Lond. A: Math. Phys. Eng. Sci. (ISSN: 1364-503X) 371 (2004), http://dx.doi.org/10.1098/rsta.2012.0358.